Generation of continental rifts, basins, and swells by lithosphere instabilities

Loïc Fourel, Laura Milelli, Claude Jaupart, Angela Limare

JOURNAL OF GEOPHYSICAL RESEARCH: SOLID EARTH, VOL. 118, 3080–3100, doi:10.1002/jgrb.50218, 2013

Generation of continental rifts, basins, and swells by lithosphere instabilities

Loïc Fourel,[1,2] Laura Milelli,[1,3] Claude Jaupart,[1] and Angela Limare[1]

Received 13 September 2012; revised 4 April 2013; accepted 8 May 2013; published 10 June 2013.

[1] Continents may be affected simultaneously by rifting, uplift, volcanic activity, and basin formation in several different locations, suggesting a common driving mechanism that is intrinsic to continents. We describe a new type of convective instability at the base of the lithosphere that leads to a remarkable spatial pattern at the scale of an entire continent. We carried out fluid mechanics laboratory experiments on buoyant blocks of finite size that became unstable due to cooling from above. Dynamical behavior depends on three dimensionless numbers, a Rayleigh number for the unstable block, a buoyancy number that scales the intrinsic density contrast to the thermal one, and the aspect ratio of the block. Within the block, instability develops in two different ways in an outer annulus and in an interior region. In the outer annulus, upwellings and downwellings take the form of periodically spaced radial spokes. The interior region hosts the more familiar convective pattern of polygonal cells. In geological conditions, such instabilities should manifest themselves as linear rifts striking at a right angle to the continent-ocean boundary and an array of domal uplifts, volcanic swells, and basins in the continental interior. Simple scaling laws for the dimensions and spacings of the convective structures are derived. For the subcontinental lithospheric mantle, these dimensions take values in the 500–1000 km range, close to geological examples. The large intrinsic buoyancy of Archean lithospheric roots prevents this type of instability, which explains why the widespread volcanic activity that currently affects Western Africa is confined to post-Archean domains.

Citation: Fourel, L., L. Milelli, C. Jaupart, and A. Limare (2013), Generation of continental rifts, basins, and swells by lithosphere instabilities, *J. Geophys. Res. Solid Earth*, *118*, 3080–3100, doi:10.1002/jgrb.50218.

1. Introduction

[2] Continental interiors have been affected by domal uplifts, volcanism, basin formation, and incipient rifting throughout their history. What has long intrigued researchers is the synchronicity of subsidence events in independent structures through a large continent. Experts on cratonic basins such as *Sloss* [1991], for example, have emphasized how upward and downward motions occur in apparently coordinated fashion over large distances. In North America (Figure 1a), the Late Proterozoic-Early Ordovician saw subsidence in four major basins, the Michigan, Illinois, Williston, and Hudson Bay, as well as the formation of major "failed" rifts such as the southern Oklahoma aulacogen and the Mississippi Valley graben (also called the Reelfoot rift) within a short time interval [*Thomas*, 2011]. North America was also affected by a series of domal uplifts at the same time, such as the Ozark and Nashville domes and the Cincinnati Arch [*Allen and Armitage*, 2012]. In similar fashion, several major basins, including the Georgina, Officer, and Amadeus, and a rift, the Adelaide geosyncline, developed simultaneously in central Australia in the Neoproterozoic about 840 Myr ago (Figure 1b) [*Lindsay et al*., 1987; *de Vries et al*., 2008]. Large-scale organization of rifting events is also obvious in Africa in the Mesozoic (Figure 1c). At that time, a system of interconnected rifts spanned the entire continent from west to east via the Central African shear zone with ramifications to the north in the Sirt rift and to the south in the Soudan and Anza rifts [*Guiraud et al*., 2005].

[3] These geological structures have been attributed to mantle convective processes or extension due to remote horizontal tectonic stresses. Models have usually been focused on individual structures and have rarely dealt with the large-scale geometrical patterns of Figure 1, which constitute important constraints in themselves. The synchronicity of rifting events, domal uplifts, and subsidence over large distances, for example, would require a set of linear upwellings and plumes striking at the same time from the deep convecting mantle. Such a complicated convection pattern is unaccounted for. Similarly, it is difficult to attribute the generation of such varied structures to a single large-scale extensional tectonic regime. This is emphasized by the three major Ordovician rifts of North America, which have

[1]Institut de Physique du Globe de Paris, Sorbonne Paris Cité, Univ Paris Diderot, Paris, France.
[2]Now at Univ. Pierre et Marie Curie, iSTeP UMR 7193 UPMC-CNRS, Paris, France.
[3]Now at EDF R&D, Département Mécanique des Fluides Energie et Environnement, Paris, France.

Corresponding author: L. Fourel, Univ. Pierre et Marie Curie, iSTeP UMR 7193 UPMC-CNRS, 4 place Jussieu, Tour 46-00, 2ieme étage, 75252 Paris cedex 05, France. (loic.fourel@upmc.fr)

2169-9313/13/10.1002/jgrb.50218

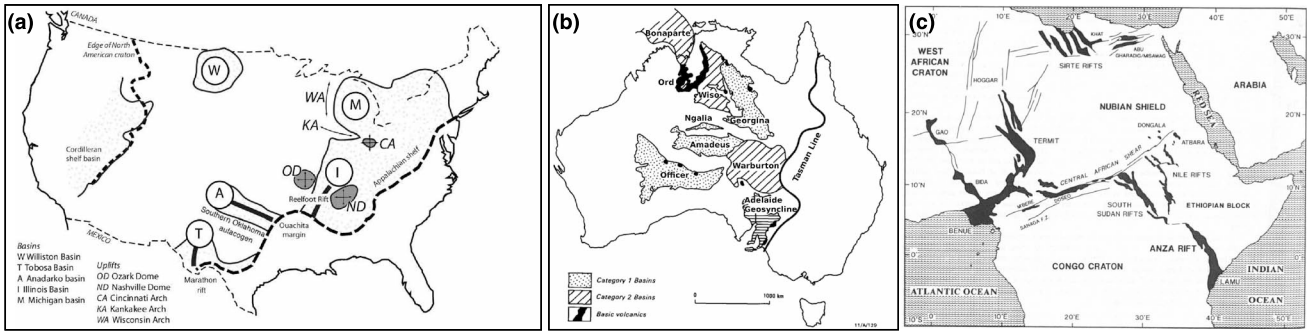

Figure 1. Three examples of contemporaneous continental rifts and basins. (a) North America in the Early Ordovician (adapted from *Allen and Armitage* [2012]). The thick dashed black lines at the east and west stand for the continent boundaries at that time. Three major rifts developed at that time: the Marathon, the southern Oklahoma aulacogen, and the Reelfoot Rift. Note that these three rifts are not parallel to one another and that they are at an approximately right angle to the local continent-ocean boundary. CA, ND, and OD stand for the Cincinnati Arch, the Ozark, and Nashville domes, three isolated swells that developed at that time. Other notable features are two uplifted arches, noted KA and WA. (b) Australia 840 Myr ago with several depocenters and the Adelaide geosyncline, which is a rift striking at a right angle to the continental edge (adapted from *Lindsay et al*. [1987]). (c) The major rifts of Africa between 140 and 70 Myr (adapted from *Bosworth and Morley* [1994]). Note the large-scale pattern and the almost throughgoing incipient rift and shear zone that almost splits the continent in two.

completely different orientations (Figure 1a). These structures are not due to preexisting zones of weakness: the southern Oklahoma aulacogen, for example, clearly cuts across the deep-seated structural grain of the North American continent [*Keller and Stephenson*, 2007].

[4] Inferring the cause of all these different tectonic events from ancient examples is difficult due to the limited number of observations that can be retrieved and it is useful to refer to Western Africa, which is active at present (Figure 2). In that region, magmatic activity occurs in a number of uplifted areas including the peculiar Cameroon Volcanic Line that extends over a distance of about 1000 km from the continental margin. Even more striking is that volcanic activity stretches across the whole continent up to the Mediterranean coast. The active volcanic centers of Western Africa outline a specific pattern that includes rifting at the continental margin and an array of domal uplifts and volcanic centers in the interior, which is reminiscent of that of North America in the Ordovician (Figure 1a). *Milelli et al.* [2012] recently summarized available information and models on the Cameroon Volcanic Line (CVL) and the underlying lithospheric mantle. Magmatic and volcanic activity has been sustained along this line for at least 70 Myr with no age progression [*Déruelle et al*., 1991]. These observations indicate that the mantle upwelling that feeds the volcanoes is not affected by absolute plate motions and hence that it is attached to the continent. Negative (low wave speed) seismic anomalies in the shallow mantle beneath the line are confined to a narrow corridor that does not extend to depths larger than 300 km, indicating that no deep mantle plume is involved [*Reusch et al*., 2010, 2011]. Eruption rates are much smaller than those of all known hot spots on Earth. *Gallacher and Bastow* [2012] have demonstrated that the Cameroon crust does not hold detectable quantities of magma so that one cannot attribute the small eruption rates to magma storage en route to the surface. Thus, the small eruption rates are due to very small magma production rates at the source and to a mantle upwelling that is anomalously slow by hot spot standards. *Ebinger and Sleep* [1998] have tried to reconcile the evidence with hot spot action and have proposed that the Afar plume "leaks" toward the west along a lithospheric basal channel, but this model is not consistent with geochronological constraints. Magmatic and volcanic activity began at about 70 Myr in Cameroon, way before the earliest trace of the Afar plume at about 45 Myr in southern Ethiopia [*Furman et al*., 2006]. Furthermore, one would expect an east-to-west age migration of volcanic activity, which is observed neither at the scale of Western Africa nor along the 1000 km long CVL. From a physical perspective, it is not clear

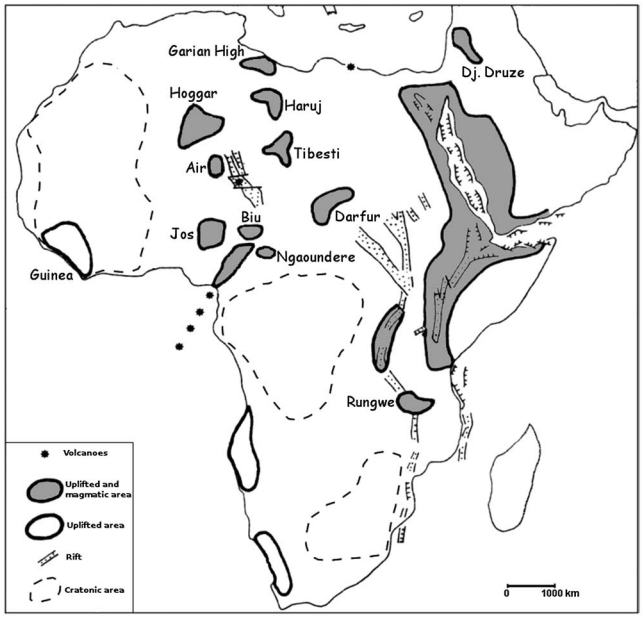

Figure 2. The active volcanic centers and swells of Africa today (adapted from *Guiraud et al*. [2005]). Note that the active centers are systematically located away from the cratons (outlined by dashed curves).

how a single plume could manage to feed volcanic activity over the vast expanses of Western Africa.

[5] The distribution of continental basins, domes, and rifts appears to follow a few simple geometrical rules. The rifts seem to develop preferentially at high angles to the edge of the continent whereas swells and basins seem confined to the interior. Other intriguing geometrical features are that the rifts often branch out in complicated patterns at their landward end. The Mississippi Valley graben, for example, segues into the Rough Creek graben at almost a right angle [*Thomas*, 1991, 2011]. At its eastern terminus, the Rough Creek graben is in turn connected to the Rome Trough graben of Kentucky and West Virginia. Studies of sedimentary strata demonstrate that these three grabens formed contemporaneously. Western Africa provides another example, with the Cameroon Volcanic Line extending to the Biu swell to the north and the Jos plateau to the west in a spectacular Y-shaped pattern (Figure 2).

[6] Physical models of continental deformation rely on driving mechanisms that are external to the continent and rarely attempt to account for episodes of widespread tectonic and magmatic activity at the scale of an entire continent. To our knowledge, no available model accounts for the shape, orientation, and distribution of the geological structures of Figures 1 and 2. Furthermore, controls on the lengths of rifts and on the spacings between volcanic centers remain unspecified. In a recent study, *Farrington et al*. [2010] have described the three-dimensional convective patterns that develop in oceanic domains away from a thick rigid lithospheric block and have emphasized the variety of structures that can be generated. Here we are interested in the structures that appear within a continent. Motivated by the observation that rifts and basins seem to develop almost simultaneously over large distances, we have sought an explanation in the continental lithosphere itself. The lithospheric mantle beneath continents has been depleted through melt extraction, which makes it buoyant with respect to the asthenosphere, but it is also colder than the asthenosphere, which may make it unstable. We show that such an instability, if it occurs, follows a spatial pattern that is comparable to the geological record. The observed planform illustrates simple geometrical controls on the flow and can be described quantitatively by a few scaling laws. Remarkable features of this type of convection are the large wavelength of the convective motions, such that a relatively thin unstable layer can generate large-scale structures, and the large periodicity between successive destabilization events, which is due to the high viscosity of the unstable lithospheric layer. The instability pattern may be of interest for other potentially unstable systems in the Earth where composition and temperature differences induce opposite changes of buoyancy, such as the large low-shear-velocity provinces that have been detected at the core-mantle boundary [*Garnero and McNamara*, 2008].

[7] Our paper is organized as follows. We first describe laboratory experiments on a "continent" of finite size, which shows that the instability pattern varies markedly and tellingly between the margins and the interior. We provide experimental scaling laws for the geometrical features of the planform and discuss the relevance for rifts and basins. Scaled to the properties and thickness of the lithospheric mantle, these characteristic dimensions are in close agreement with the observations. We discuss the physical conditions that are required for the mechanism to operate and generate the geological structures that are observed at Earth's surface. We argue that the very specific spatial pattern of Figures 1 and 2 provides a stringent reality check on physical models for continental tectonics. We show at the end of the paper that our model can account for several other important features of rifting and subsidence events, such as the apparent synchronicity of basin formation in different landmasses following the breakup of a supercontinent and the avoidance of rifting in certain parts of western Africa today.

2. Physical Framework

[8] Continental lithosphere may be as thick as 180 km to 250 km over lateral distances of 5000 to 10,000 km beneath Archean cratons and Proterozoic provinces. It is chemically depleted, intrinsically buoyant, refractory, dehydrated, and submerged in asthenospheric mantle that is both hotter and less viscous than it is. It may become unstable due to cooling, depending on the magnitudes of the intrinsic and thermal density contrasts that are involved. The opposite situation is found in the large low-shear-velocity provinces that lie at the core-mantle boundary, which are probably stabilized because they are made of intrinsically dense mantle and which may go unstable due to heating from below by the core. Ignoring viscosity variations due to temperature, the two cases are dynamically equivalent.

2.1. Stability and Instability of a Thin Layer Submerged in a Deep Fluid

[9] In this initial study, there are no viscosity variations due to temperature, but we allow for such variations when evaluating geological conditions. *Jaupart et al*. [2007] have documented in detail the behavior of a layered system. In this case, thermal steady state can be achieved with small-scale convection supplying heat that is conducted through the buoyant layer, but it may be dynamically unstable. Figure 3 defines the different layers involved and their geological analogs. Two dimensionless numbers are sufficient to characterize the dynamics in geological conditions, the Rayleigh number Ra for the buoyant layer and the buoyancy number B

$$Ra = \frac{\Delta\rho_T g h_d^3}{\kappa\eta_1}, \tag{1}$$

$$B = \frac{\Delta\rho_c}{\Delta\rho_T}, \tag{2}$$

where h_d is the buoyant layer thickness, g is the acceleration of gravity, $\Delta\rho_T$ is the thermal density contrast ($\equiv \rho_0\alpha\Delta T$, where ρ_0 is the buoyant layer density, ΔT is the temperature difference across the buoyant layer, and α is the thermal expansion coefficient), κ is thermal diffusivity, and η_1 is the viscosity of the buoyant layer material. The intrinsic density contrast, $\Delta\rho_c$ ($\equiv \rho_M - \rho_0$ where ρ_M is the density of the deeper layer), is due to composition and, in the case of continents, to melting and melt extraction. Three other dimensionless numbers appear in the governing equations, the Prandtl number (η_1/κ), the viscosity ratio between the buoyant layer and the lower fluid ($\gamma = \eta_1/\eta_2$), and the ratio of total fluid depth to buoyant layer thickness, but they do not affect the results significantly if they take the large values that are relevant to geological cases [*Jaupart et al*., 2007]. Motions in the deep fluid take the form of small-scale convection below the interface with negligible dynamic impact on the stability or

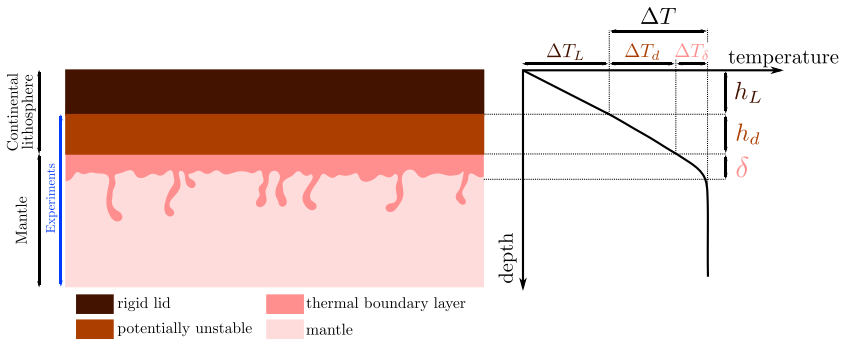

Figure 3. Definition of the different thicknesses and temperature contrasts involved in a buoyant layer and underlying fluid that are cooled from above. h_d is the thickness of the depleted mantle that can potentially become unstable at the base of the lithospheric mantle, δ is the thickness of the asthenospheric thermal boundary layer below it, and ΔT is the total temperature difference across these two layers ($\equiv \Delta T_d + \Delta T_\delta$).

instability of the buoyant upper layer due to the large separation of scales (Figure 3).

[10] Using both theory for marginal stability and laboratory experiments, *Jaupart et al*. [2007] showed that the critical Rayleigh number for instability depends strongly on the buoyancy number, from $Ra_c \sim 28$ at low values of B to $Ra_c \sim 1100$ for $B \geq \approx 0.5$. Two different types of convective motions can occur depending on the B value. For $B < 0.5$, instability proceeds through the intermittent release of downgoing plumes of upper fluid that protrude into the lower fluid and come back up. This generates large thickness variations in an array of basins and swells in the buoyant upper layer. For $B > 0.5$, the upper layer undergoes internal convective overturn with little deformation of its base. We evaluate the values of *Ra* and *B* that are relevant for the continental lithosphere in a separate section (see section 4.1).

[11] It is the first, oscillatory, instability regime that is most relevant and most interesting for geology, because of its remarkable features. The very small values of the critical Rayleigh number emphasize the highly unstable nature of the thermal stratification, such that even strong dehydrated lithospheric mantle can get destabilized. Due to their geometrical setup, with the buoyant upper layer extending throughout the experimental tank, the experiments of *Jaupart et al*. [2007] could not document the instability pattern at the edge of an unstable block and this study was aimed at filling this gap.

2.2. Convective Instability of a Block of Finite Width

[12] Consider a homogeneous buoyant block of finite width with no vertical change of composition and intrinsic density over thickness h_d at the top of a larger volume of fluid, such that there are density and viscosity variations in both the horizontal and vertical directions. We shall consider blocks of different sizes in order to document the impact of the thickness-to-width ratio h_d/R, where R is the half-width of the block. For convenience, we shall refer to h_d/R as the aspect ratio of a block. Due to cooling from above, the blocks develop instabilities that manifest themselves by thickness variations in the form of linear, radially oriented, ridges and furrows as well as basins and swells. To our knowledge, no experimental or theoretical studies have documented the instability pattern and threshold in such a configuration.

[13] For reference, we briefly review a few studies that illustrate the impact of lateral boundaries on the convection planform in cylindrical tanks. In these studies, rigid tank walls impose no-slip boundary conditions at the edges of the unstable layer. In a Rayleigh-Benard configuration, with fixed temperatures at the top and bottom, three dimensionless numbers characterize the dynamics of convection: the Prandtl and Rayleigh numbers, which have already been defined, and the aspect ratio h/R, where h and R are the height and radius of the cylinder, respectively. For our present purposes, we need only refer to large Prandtl number fluids and aspect ratios that are much less than 1, typically 0.1. The critical Rayleigh number for the onset of convection increases with this ratio, according to both theory [*Charlson and Sani*, 1970, 1971; *Rosenblat*, 1982] and experiments [*Stork and Müller*, 1975]. Different planforms are generated depending on the thermal boundary conditions at the side walls. For conducting walls with horizontal temperature gradients in the radial direction, convection develops as a set of concentric circular upwellings and downwellings [*Koschmieder*, 1966]. For insulating boundary conditions, *Croquette et al*. [1983] found that disordered planforms prevail. He emphasized that near the sidewalls, upwellings and downwellings develop in a direction perpendicular to the walls and branch out in a complex polygonal planform in a central region. We shall find a degree of similarity with these experimental findings. *Croquette et al*. [1983] did not attempt to determine the lengths and branching patterns quantitatively as a function of the governing parameters, which does not allow extrapolation to other cases.

[14] With respect to these older laboratory experiments, our study involves three other dimensionless numbers, the buoyancy number B, of course, the viscosity ratio between the block and the lower fluid ($\gamma = \eta_1/\eta_2$), and the ratio of total fluid depth to block thickness. As stated above, the latter two ratios, however, do not affect the results significantly if they take the large values that are relevant to geological cases. One additional factor is the shape of the block. We have used mostly disk-shaped blocks of radius R but have carried out a few control experiments with square blocks.

[15] We have used aspect ratios in a [0.01–0.1] range, which is appropriate for Earth. The smallest continent of today, Australia, stretches over 1800 km from north to south, corresponding to a half-width of 900 km. For an average

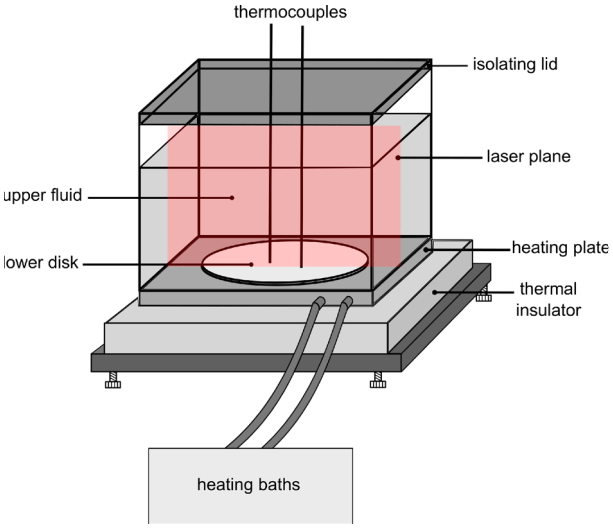

Figure 4. Experimental setup. The tank has a 30 cm × 30 cm square horizontal cross-section and is 20 cm high. Tank walls are made of 3 cm thick Plexiglas to minimize heat losses to the room.

thickness of unstable lithospheric mantle of 50 km (see section 4.1), $h_d/R \sim 0.06$. At the other extreme, a supercontinent such as Pangaea occupied about 30% of Earth's surface, corresponding to an aspect ratio of about 0.01.

[16] We have focused on buoyancy numbers in a narrow range around 0.25 in order to keep the number of variables and experiments to a manageable amount. *Poudjom Djomani et al*. [2001] have suggested that the degree of chemical depletion varies systematically with the age of the continent, such that Archean cratons are the most depleted and hence have the largest intrinsic density contrast. For continental lithosphere, therefore, the buoyancy number probably increases with age. We shall argue below that it is likely to be as small as 0.25 for Proterozoic provinces. We carried out a few experiments at larger values of B, corresponding to older continental lithosphere, to check that the same spatial pattern was obtained. Although the basic features of the instability planform are not sensitive to B, the likelihood of convective breakdown, as measured by the value of the critical Rayleigh number for instability, depends strongly on the buoyancy number [*Jaupart et al*., 2007].

2.3. Experimental Setup

[17] As already mentioned, we do not allow for significant variations of viscosity with temperature in these experiments in order to deal with a small set of control parameters. In this case, heating a dense block from below is equivalent to cooling a buoyant block from above, but the former is much simpler to study in a laboratory than the latter. One reason is that it is difficult to prepare buoyant liquids with densities that can be varied within a large range. Another reason is that it is more convenient to image the flow pattern from above than from below. We used miscible fluids to avoid surface tension effects that are absent in geological cases. Experimental fluids were mixtures of hydroxyethyl cellulose, ammonium chloride salt, and water. Cellulose and salt were used to set viscosity and density, respectively [*Tait and Jaupart*, 1989]. Fluid properties were measured in the laboratory prior to each experiment. For the small deformation rates of our experiments, our home-made mixtures behave as Newtonian liquids. Over the temperature range of this study, their viscosities vary weakly with temperature, typically by 25% for a temperature difference of 25 K. For each experiment, viscosity values are listed at the average temperature, as appropriate for variable viscosity fluids [*White*, 1988].

[18] The experimental setup is shown schematically in Figure 4. The tank had dimensions of $0.3 \times 0.3 \times 0.2$ m in the horizontal and vertical directions, respectively, with 30 mm thick Plexiglas walls that allowed good thermal insulation. This tank rested on a copper plate through which thermostated water was circulated. We took special care to achieve a constant and uniform basal temperature. Following a short transient initial heating, basal temperature variations were always less than 0.1°C in both space and time, which was a negligible fraction of the overall temperature difference across the fluid layers (typically 25°C). The top of the upper fluid was a free surface in contact with air below a thick Plexiglas plate which insulated it from the laboratory. Two sets of six thermocouples recorded vertical temperature profiles in two locations every 5 s with an accuracy of 0.1°C. Three additional thermocouples monitored temperatures in the basal copper plate and outside the tank. Small tracers were added to the dense fluid which was periodically illuminated with a laser device in a planar vertical cross section.

2.4. Experimental Protocol

[19] Each experiment followed the same protocol. The tank was filled with the lighter fluid (distilled water for most experiments) and a fixed volume of the denser fluid was rapidly poured onto the base using a small tube located at the center. The dense fluid was allowed to spread until no significant change of radius could be detected over a time equal to the duration of an experiment, which was typically 1 h. Details on the shape of the potentially unstable block and its spreading rate are given in section A. All the dense blocks had the same shape in cross section when instability set in, regardless of the viscosity ratio between block and ambient fluid, such that thickness variations were only marked in a narrow outer margin. Once the spreading rate of the dense fluid was negligible (see section A), we imposed a very rapid temperature change at the base of the tank (typically 1 min) using a set of interconnected heating baths. This was done to ensure that instabilities did not begin before the end of the transient ramp-up in basal temperature. Due to heating from below, the overall density contrast between the "continent-like" block and surrounding fluid decreased and no significant change of radius was observed during the course of an experiment. We carried out a total of 80 experiments and report on a large subset of them, with characteristics that are listed in Table 1. They are labeled ASTICO, an acronym for Analysis of Stability and Instability of Continents, a slightly misspelled French word for maggot.

[20] In the vast majority of experiments, the dense fluid had an almost perfect circular outline in the horizontal plane and a flat domal shape in vertical cross section. Radius R was measured from photographs to within 2%. The mean thickness, h_d, of the block was calculated using the radius R and the known volume V, assuming an equivalent cylindrical

Table 1. List of Experiments Used in This Study and Their Parameters[a]

Name	Geometry	Ra	B	$\overline{h_d}$ (cm)	h_d/R	$\eta(1)/\eta(2)$	Regime
ASTICO 02	disk	141	0.244	0.56	0.0503	690	unstable
ASTICO 03	disk	203	0.248	0.63	0.0515	670	unstable
ASTICO 04	disk	430	0.220	0.76	0.0572	630	unstable
ASTICO 07	disk	244	0.678	0.53	0.0371	410	stable
ASTICO 15	disk	234	0.231	0.79	0.0651	1320	stable
ASTICO 16	disk	286	0.225	0.83	0.0694	1290	stable
ASTICO 17	disk	198	0.243	0.77	0.0903	1330	stable
ASTICO 20	disk	440	0.224	0.96	0.0713	1270	transitional
ASTICO 23	disk	617	0.194	0.9	0.0715	720	unstable
ASTICO 24	disk	404	0.227	0.85	0.0657	790	unstable
ASTICO 26	disk	172	0.342	0.76	0.0532	870	stable
ASTICO 28	disk	226	0.231	0.69	0.0594	750	transitional
ASTICO 29	disk	314	0.233	0.78	0.0640	780	transitional
ASTICO 30	disk	164	0.250	0.66	0.0672	810	stable
ASTICO 31	disk	154	0.249	0.63	0.0682	770	stable
ASTICO 32	disk	361	0.210	0.88	0.0742	1160	stable
ASTICO 33	disk	426	0.202	0.89	0.0736	1060	transitional
ASTICO 34	disk	29	0.213	0.38	0.0367	1150	transitional
ASTICO 35	disk	266	0.207	0.75	0.0659	890	transitional
ASTICO 36	disk	304	0.217	0.78	0.0644	830	transitional
ASTICO 38	disk	321	0.240	0.79	0.0615	970	unstable
ASTICO 39	disk	268	0.241	0.73	0.0555	930	unstable
ASTICO 40	disk	59	0.252	0.46	0.0546	990	transitional
ASTICO 41	disk	385	0.242	0.82	0.0649	900	unstable
ASTICO 42	disk	121	0.226	0.62	0.0585	1100	transitional
ASTICO 43	disk	309	0.219	0.88	0.0715	1380	stable
ASTICO 44	disk	75	0.231	0.56	0.0751	1400	stable
ASTICO 45	disk	103	0.215	0.34	0.0281	170	unstable
ASTICO 47	disk	28	0.208	0.22	0.0209	170	unstable
ASTICO 48	disk	32	0.249	0.25	0.0219	180	unstable
ASTICO 49	disk	4	0.251	0.38	0.0498	8120	stable
ASTICO 51	disk	103	0.213	0.34	0.0282	170	unstable
ASTICO 52	disk	80	0.205	0.46	0.0366	550	unstable
ASTICO 53	disk	75	0.207	0.45	0.0347	570	unstable
ASTICO 54	disk	44	0.212	0.28	0.0282	570	unstable
ASTICO 55	disk	91	0.210	0.48	0.0370	560	unstable
ASTICO 56	disk	96	0.220	0.5	0.0387	560	unstable
ASTICO 57	disk	148	0.207	0.55	0.0445	510	unstable
ASTICO 61	square	21	0.221	0.33	0.032	850	unstable
ASTICO 69	disk	203	0.213	0.66	0.0476	450	unstable
ASTICO 70	disk	30	0.242	0.34	0.0267	150	unstable
ASTICO 71	disk	43	0.244	0.26	0.0190	160	unstable
ASTICO 72	disk	43	0.238	0.26	0.0190	160	unstable
ASTICO 73	disk	44	0.229	0.26	0.0190	160	unstable
ASTICO 74	disk	79	0.229	0.31	0.0250	160	unstable
ASTICO 75	disk	41	0.229	0.25	0.0200	160	unstable
ASTICO 76	disk	24	0.229	0.21	0.0160	160	unstable
ASTICO 77	square	74	0.290	0.33	0.033	160	unstable

[a]For square-shaped experiments, R is the half size of the square.

shape ($V = \pi R^2 h_d$). The uncertainty on h_d is therefore 4% and the corresponding uncertainty on the aspect ratio is 6% at most. Density values and temperatures were measured accurately, such that the uncertainty on the buoyancy number, B, was $\approx 1\%$. The uncertainty on the Rayleigh number, Ra, was larger, due to potential errors on all the input variables, and could be as large as 12%.

[21] For each experiment, time $t = 0$ is set at the beginning of heating and time is made dimensionless using the diffusion time scale for the block, $t_{\text{diff}} = h_d^2/\kappa$. h_d is used to scale height above the base of the tank. Temperature differences are scaled to ΔT, such that $T' = (T - T_0)/\Delta T$, where T_0 is the initial temperature of both fluids. In the following, we drop the primes for convenience and quote all variables in dimensionless form.

3. Experimental Results

[22] The time sequence of a typical experiment is as follows. Small-scale convection rapidly developed in the outer fluid due to its low viscosity. At small times, this form of convection was only active where the ambient fluid was in direct contact with the heated tank base, and did not appear at the top of the block which was still at its initial temperature. Heat eventually diffused to the top of the block and generated a thin boundary layer in the ambient fluid which also drove small-scale convection, albeit with a smaller temperature difference than at the tank base. We took special care to identify the effects of small-scale convection in the ambient fluid in order to separate it from the second, and more interesting, form of convection, which arises from the unstable thermal stratification of the dense fluid. Typically, small-scale convection was intermittent

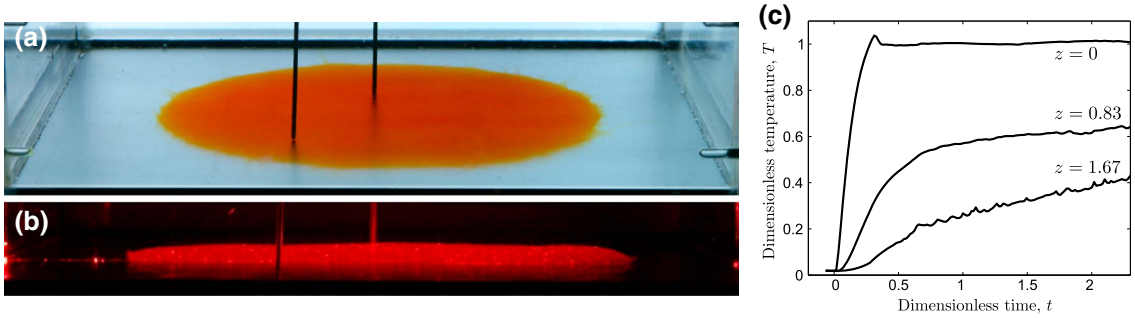

Figure 5. Stable experiment ASTICO 30 ($Ra = 164, B = 0.25, h_d/R = 0.067$). (a) Photograph in normal light. Total width of view is 30 cm. (b) Laser vertical cross section. (c) Time evolution of temperatures at three different depths. Height z is scaled to the unstable block thickness. Temperature fluctuations are only significant in the ambient fluid and are due to small-scale convection.

and unsteady due to the large Rayleigh number that characterizes the low-viscosity ambient fluid, and manifested itself through thin wisps or streaks that could be visualized easily in shadowgraph.

3.1. Stability Diagram

[23] We have defined three distinct regimes in our experiments: a stable one, an unstable one, and a transitional one close to marginal stability conditions. Each experiment was attributed to one of these regimes after careful scrutiny of photographs and temperature records. There was always small-scale rapid convection in the ambient fluid, independently of the behavior of the block itself.

[24] The stable regime is characterized by no detectable deformation of the interface between the two fluids save for the thin colored wisps due to small-scale convection. The morphology of the block does not change through time. Figure 5a shows a photograph of one experiment in this regime, ASTICO 30, at $t = 1$. The dense "continent-like" block has a flat domal shape with slight entrainment of fluid at its leading edges. The laser vertical cross section in Figure 5b confirms the absence of interface deformation. Figure 5c shows how temperatures evolve in the copper plate ($z = 0$), within the block ($z = 0.83$), and in the surrounding fluid ($z = 1.67$). Note that the basal temperature is stabilized at an approximately constant value after a very short transient. Temperatures within the block increase slowly due to diffusion. Small-scale convection sets in the upper fluid at $t \approx 0.6$ as shown by the small and rapid temperature fluctuations that appear immediately above the block at that time.

[25] The unstable regime is characterized by major deformations of the interface between the two fluids. We arbitrarily define this regime to be such that thickness variations are at least 10% of the initial h_d value. By the end of an experiment in this regime, the block either is lumpy or has completely disappeared due to mixing with the surrounding fluid. Figure 6a shows a photograph that illustrates the main features of this regime for experiment ASTICO 24 at $t = 1$. We can see horizontal variations of color contrast due to thickness variations within the block. Swells and basins are conspicuous in the vertical laser cross section of Figure 6b. One noteworthy feature of the temperature record is a kink at $z = 0.65$ and $t = 0.8$ (Figure 6c). At that time, a basin had developed at the thermocouple location and colder upper fluid had penetrated almost to the base of the tank. In experiments with major disruption or mixing of the unstable block, temperature fluctuations are even larger than shown here. The amplitudes of interface deformation and temperature oscillations increase with the Rayleigh number, i.e., with increasing distance from the stability curve, and provide us with a method to estimate the critical Rayleigh number, Ra_c.

[26] The threshold between stability and instability could not be determined accurately using our laboratory setup. We defined instead a transitional regime, such that the interface deformation is a small fraction of the initial block thickness (<10%) and the block keeps the same shape in both vertical and horizontal cross sections. Since the amplitude

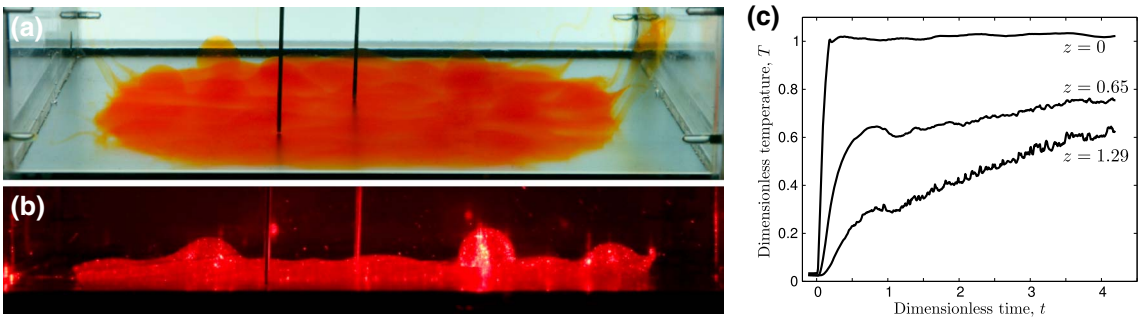

Figure 6. Unstable experiment ASTICO 24 ($Ra = 404$, $B = 0.23$, $h_d/R = 0.066$). (a) Photograph in normal light. (b) Laser vertical cross section. (c) Time evolution of temperatures at three different depths. Note the temperature fluctuations that develop at midheight above the tank base, due to thinning of the dense basal block.

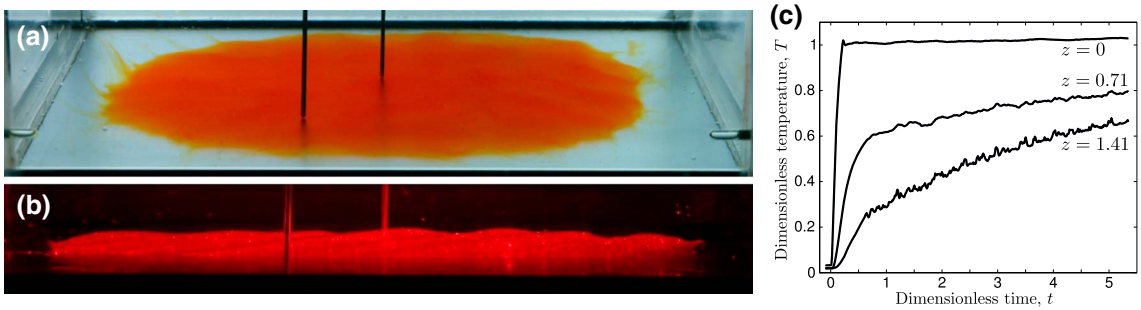

Figure 7. Transitional experiment ASTICO 29 ($Ra = 314$, $B = 0.23$, $h_d/R = 0.064$). (a) Photograph in normal light. (b) Laser vertical cross section. (c) Time evolution of temperatures at three different depths.

of instabilities increases with Ra/Ra_c, transitional experiments are as close to marginal stability as our detection abilities allow. Figure 7a shows the apparently undeformed disk of experiment ASTICO 29 at $t = 1$. The laser vertical cross section, however, reveals small deflections of the interface (Figure 7b), and the temperature data in Figure 7c clearly exhibit a departure from the initial diffusion trend. In the transitional regime, the dense block ends up with the same shape and dimensions as at the beginning once heating is stopped. For both the unstable and transitional regimes, note that there are two types of convection: a large-scale one due to the slow and periodic breakdown of the dense block and a small-scale and rapid one in the ambient fluid.

[27] We have focused on a narrow range of buoyancy numbers around 0.25 and explored large ranges of values for the Rayleigh number and the aspect ratio of the block. The regime diagram is shown in (h_d/R, Ra) space in Figure 8. The stability curve is drawn between the stable experiments and the transitional ones, allowing for some uncertainty on the values of both Ra_c and h_d/R. The stability diagram can be split further in two different parts. For aspect ratios lower than 0.05, the critical Rayleigh number is very small (~30) and approximately equal to the value for the layered configuration [*Jaupart et al.*, 2007], corresponding to the limit of vanishing h_d/R. For these experiments, the finite width of the unstable block does not affect the stability threshold. Ra_c increases dramatically with h_d/R for aspect ratios larger than 0.05 and exceeds 500 for $h_d/R > 0.07$. A similar trend has been found for Rayleigh-Benard convection in cylindrical tanks [*Rosenblat*, 1982; *Stork and Müller*, 1972, 1975].

3.2. Instability Planform

[28] The peculiar planform of convective instabilities in a disk is shown schematically in Figure 9. In the central part of the disk, the pattern is made of polygonal cells, which is analogous to that for an unstable layer [*Jaupart et al.*, 2007]. At the edges of the disk, instabilities appear as radial straight spoke-like upwellings and downwellings. The transition between these two patterns is achieved via Y-shaped junctions. One can easily understand why the radial pattern cannot be sustained throughout the disk, from the edge to the center: if it did extend to the center, the spacing between upwellings and downwellings would decrease to zero, which would lead to shear over vanishing regions and hence very large viscous stresses that could not be sustained. Linear

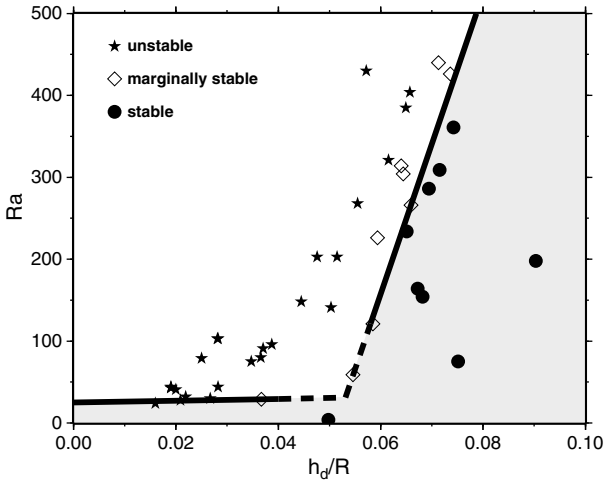

Figure 8. Stability diagram in ($h_d/R, Ra$) space. Circles, diamonds, and stars represent stable, transitional, and unstable experiments, respectively. The stable domain is shaded in grey. The dashed part of the marginal stability boundary is not tightly constrained.

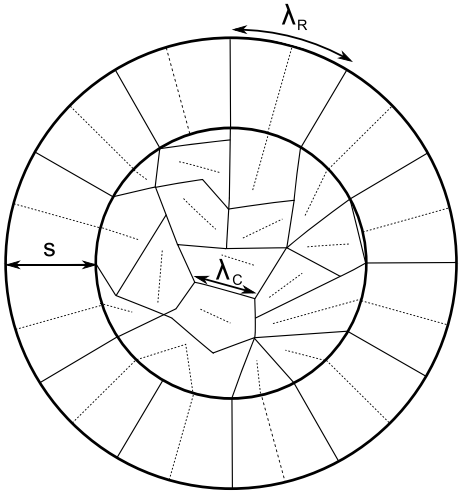

Figure 9. Schematic diagram illustrating the main features of the convection planform. Radial spokes separated by distance λ_R are in an outer rim of width s. Polygonal cells with edges of length λ_C lie within an inner circular domain. Full and dashed lines illustrate the axes of upwellings and downwellings.

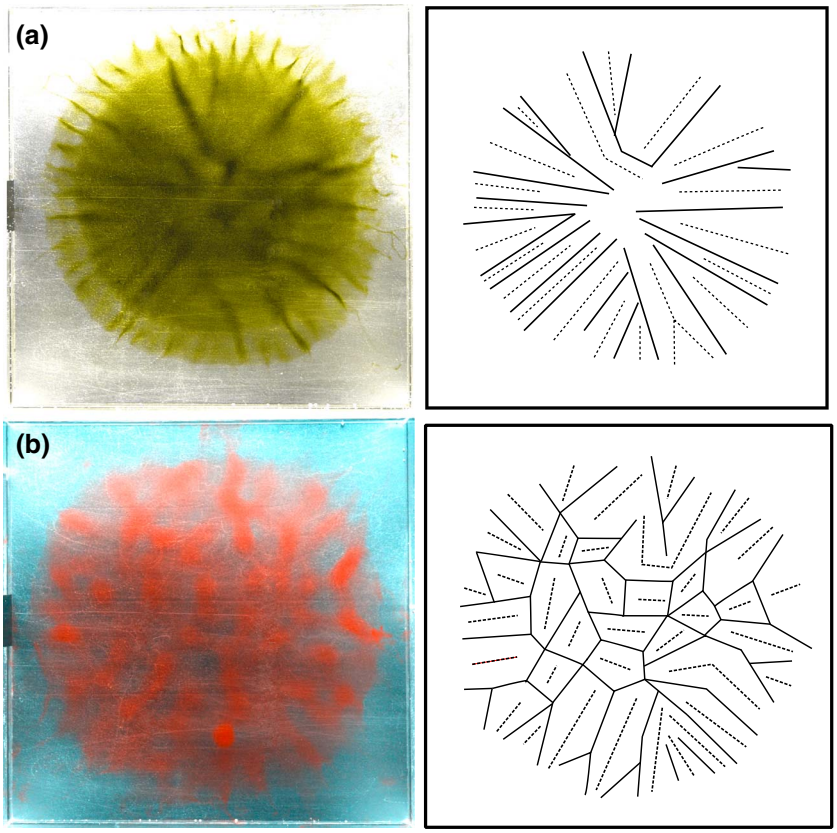

Figure 10. (a) An experiment with small inner domain exhibiting well-marked radial structures, ASTICO 75 ($Ra = 41, B = 0.23, h_d/R = 0.02$) at $t = 2.4$. (b) An experiment with a large inner domain showing the complicated polygonal inner pattern ASTICO 69 ($Ra = 203, B = 0.21, h_d/R = 0.048$) at $t = 1$.

spoke upwellings must be fed by lateral fluid flow, which would not be effective over small distances.

[29] The radial spoke planform is limited to an outer annulus of width s and is clearly periodic. We denote by λ_R the distance that separates two adjacent upwellings (Figure 9). These two characteristic distances vary with the aspect ratio of the unstable block. As shown in Figures 10a and 10b, a large number of radial spokes develop across a large annulus in the block with the smallest aspect ratio investigated ($h_d/R = 0.02$). In that block, the central polygonal pattern is only developed over a small axial domain (i.e., s/R takes a large value, ~0.8). This is in marked contrast with the planform at a larger value of h_d/R (=0.048), as illustrated in Figure 10b. In that case, the outer radial pattern is limited to a thinner annulus ($s/R \sim 0.5$) and the instability planform is dominated by a polygonal network with small swells growing at the nodes.

[30] The radius of the block does not change significantly in the course of an experiment and is therefore used to scale all dimensions. To determine s, the width of the outer annulus with predominantly radial structures, we have traced each linear spoke and measured the distance at which there is a measurable deviation from a radial trajectory. The average value is our best estimate of s. Arc lengths between two adjacent spokes can be measured directly or by dividing the outer perimeter of the disk-shaped block by the number of spokes. This provides a value for λ_R. The central polygonal region is more difficult to analyze due to the complicated pattern and the variable intensity of color contrasts. The pattern is evolving with time with some cells that merge with neighboring ones, so that some edges may be too faint for clear-cut identification. Visual inspection indicates a mixture of squares and hexagons. To base this on firmer ground, we counted the number of edges that converge to a vertex and found either threes or fours. We determined a characteristic length scale, noted as λ_C, using two different methods, by measuring the length of well-defined edges and by dividing the area of the central region, a circle of radius equal to $(R - s)$, by the number of cells. Both methods led to values within 10% of one another. From the geometrical properties of hexagons, the distance between the centers of two adjacent cells is equal to $\sqrt{3}\lambda_C \approx 1.7\lambda_C$. In several experiments, the number of well-developed cells in the axial domain was small, in which case the notion of a periodic spatial structure is questionable. Furthermore, this did not allow good statistics on the values of λ_C.

[31] By analogy with the wavelength of Rayleigh-Benard cells, which decreases as the Rayleigh number increases, we expect that the characteristic dimensions of our convective structures depend on the Rayleigh number. We cannot measure these dimensions right at marginal stability because the pattern is not really visible, so we can only work at supercritical values of Ra. We measured these geometrical characteristics for experiments that were not too far from marginal stability, which we define to be such that $Ra/Ra_c < 5$ (Table 2). We may thus expect some scatter due to the range of Rayleigh numbers that was used. For application to the geological record, however, we only need approximate estimates and the experimental

Table 2. List of Experiments Close to Marginal Stability and the Characteristic Dimensions of Their Spatial Patterns[a]

Name	Ra/Ra_c	λ_R/R	λ_C/R	s/R
ASTICO 23	1.67	0.27	0.00	0.30
ASTICO 24	1.54	0.36	0.31	0.29
ASTICO 36	1.28	0.32	0.29	0.43
ASTICO 38	1.73	0.33	0.26	0.42
ASTICO 39	3.57	0.27	0.00	0.48
ASTICO 45	3.66	0.14	0.20	0.89
ASTICO 47	1.02	0.17	0.23	0.88
ASTICO 48	1.16	0.15	0.00	0.89
ASTICO 53	2.59	0.20	0.28	0.58
ASTICO 54	1.56	0.17	0.20	0.57
ASTICO 57	4.93	0.27	0.31	0.60
ASTICO 61	1.0	0.19	0.31	0.56
ASTICO 70	1.07	0.19	0.25	0.53
ASTICO 73	1.62	0.16	0.00	0.94
ASTICO 75	1.50	0.12	0.20	0.81
ASTICO 76	1.0	0.13	0.19	0.81
ASTICO 77	2.58	0.19	0.24	0.73

[a] $\lambda_C = 0$ when it was too difficult to measure it properly.

scatter was found to be quite small. Our data show that the dimensionless wavelength of the initial instability, λ_R/R, is proportional to h_d/R (Figure 11), indicating that the wavelength scales in fact with the block thickness h_d. The best fitting relationship is such that $\lambda_R \approx 5.3 h_d$.

[32] The width of the outer annulus with a radial pattern decreases with increasing aspect ratio (Figure 12). The relationship can be understood using a simple argument. In the outer region, the number of spokes decreases inward via Y-shaped junctions until one reaches the interior polygonal region. For a set of radial spokes to segue into a polygonal array, there must be a minimum number of spokes. Let n denote the number of spokes at the transition between the two patterns. $n = 2$ corresponds to only one diametrical spoke across the circle, which does not allow any branching to a polygonal pattern. For a hexagonal pattern, the simplest configuration has a single central cell connected to six radial spokes, such that $n = 6$. This bare-bones figure, however, does not match our observations, which indicate a more complex central polygonal array. We require that the perimeter of the inner region, i.e., the length of the circular boundary separating the inner and outer regions with different instability patterns, must be such that it accommodates a fixed number of cells. This boundary hovers around a circle of radius $(R - s)$. Thus, assuming that all lengths scale with the peripheral spoke spacing, λ_R, we may write

$$2\pi(R - s) = n\lambda_R. \tag{3}$$

[33] Setting $\lambda_R = \beta h_d$, where $\beta \approx 5.3$, as shown above, we can rewrite equation (3) as follows:

$$\frac{s}{R} = 1 - \frac{\beta n}{2\pi}\frac{h_d}{R} \sim 1 - 0.84n\frac{h_d}{R}. \tag{4}$$

[34] The data are consistent with a relationship of this form (Figure 12), with the following best fit coefficient:

$$\frac{s}{R} \approx 1 - 10\frac{h_d}{R}, \tag{5}$$

corresponding to $n \sim 12$. This relation implies that the largest aspect ratio for this type of radial instability pattern is $(h_d/R)_{\max} \approx 0.1$.

[35] Measurements of the characteristic size of polygonal cells in the interior region exhibit more scatter than those of the peripheral spoke spacing. We attribute this to the small number of cells that can develop, which has two consequences. One is that the pattern cannot be perfectly periodic due to space limitations and the requirement of connecting cell vertices to radial spokes. Another consequence is that a single anomalous cell can impact the statistics. We have stated above that the cells are mostly hexagons or squares on the basis of the number of vertices, but we also observed a few pentagons and a few cells that could not be reduced to canonical forms. We found that the average cell edge, λ_C, tends to be significantly larger than λ_R when there are only a small number of fully developed cells in the central region. With more than four such cells in the interior, values of λ_C are comparable to those of λ_R (Figure 13).

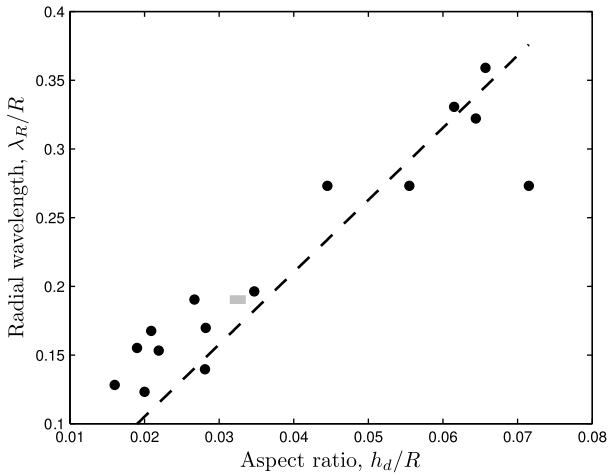

Figure 11. Dimensionless spacing between outer radial spokes, λ_R/R, as a function of disk aspect ratio. Black dots and grey squares stand for experiments in disk-shaped and square-shaped unstable blocks, respectively. The standard deviation on these values typically amounts to 10%. The best fit dashed line is such that $\lambda_R/R = 5.3 h_d/R$.

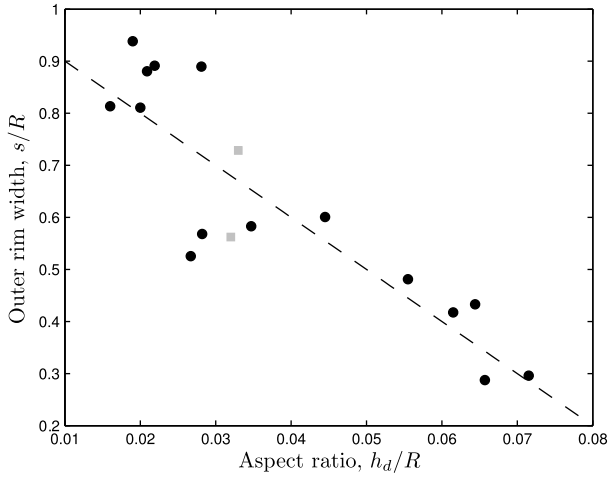

Figure 12. Dimensionless outer annulus width, s/R, as a function of aspect ratio. The dashed line stands for equation (5). Black dots and grey squares stand for experiments in disk-shaped and square-shaped unstable blocks, respectively.

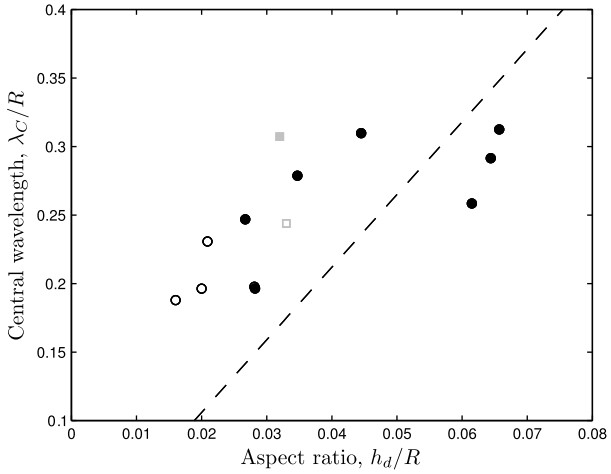

Figure 13. Dimensionless lengths of inner polygon edges, λ_C/R, as a function of aspect ratio. Circles and squares stand for experiments in disk-shaped and square-shaped unstable blocks, respectively. Open circles and square correspond to experiments with fewer than four well-developed polygons in the inner domain. The dashed line indicates the best fitting relationship for λ_R/R. Note that the cell dimensions are systematically larger with only a few polygons present.

Consequently, we will use the best fit on measurements of λ_R to evaluate λ_C in the following.

3.3. Time-Dependent Evolution

[36] The time evolution of convection depends on Ra/Ra_c. At large supercritical values of the Rayleigh number ($Ra/Ra_c \gg 10$), vigorous flow leads to rapid mixing between the two fluids and the unstable block eventually disappears. Close to marginal stability, flow is slower and we could not measure any significant change of volume and/or thickness for the block. In that case, the planform evolution is illustrated in Figure 14. We can see that the unstable block has not spread horizontally and that its radius has not changed. The width of the outer annulus which hosts radial structures does not change either, but the pattern clearly coarsens, with both λ_R and λ_C increasing with time as shown in Figure 15. In this particular example, both wavelengths increase by a factor of 1.5 in $6t_{\text{diff}}$. This process involves the lateral migration of the edges of some cells due to stronger flow in adjacent cells. One can see in the bottom part of Figure 14 that some cells have grown at the expense of neighboring ones. The quickness of such rearrangements increases with the value of Ra/Ra_c.

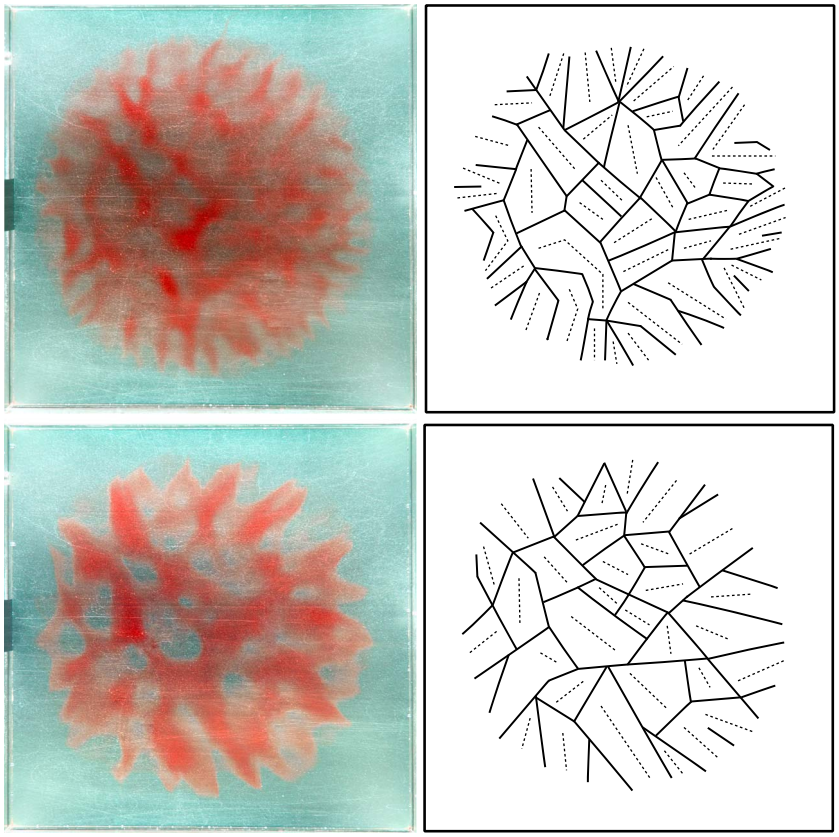

Figure 14. Instability planform for experiment ASTICO 70 ($Ra = 30, B = 0.24, h_d/R = 0.027$) at (top) $t = 3.8$ and (bottom) $t = 9.8$. Note the coarsening of the pattern.

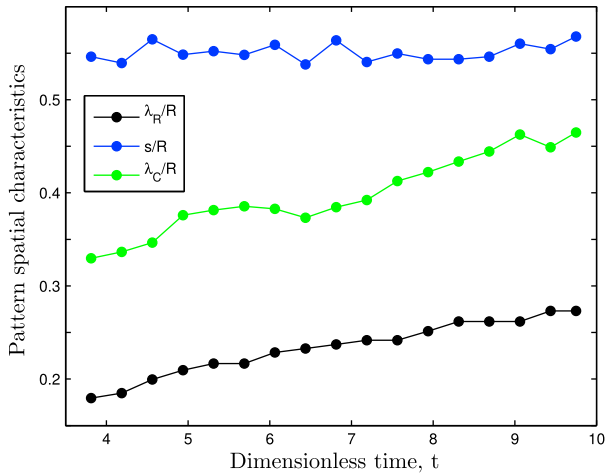

Figure 15. Time evolution of the characteristic dimensions of the instability pattern for ASTICO 70 ($Ra = 30$, $B = 0.24$, $h_d/R = 0.027$).

3.4. Experiments With Square-Shaped Unstable Blocks

[37] Our experiments have dealt mostly with circular blocks because this shape does not introduce any geometrical complexity and allows the periodic planform to manifest itself in the most conspicuous manner. There is no such thing as a circular continent, however, and we have conducted experiments with square blocks in order to assess the shape impact.

[38] Figure 16 shows that the instability planform shares many features with those for a disk, with a marked difference of pattern between an outer fringe with linear upwellings (and associated downwellings) and an inner region with polygonal cells. Many spokes do not reach the center and terminate in Y-shaped junctions. As for circular blocks, the instability wavelength increases with increasing Rayleigh number. The spoke-like upwellings of the outer region are not perpendicular to the edge of the block everywhere but maintain a global radial arrangement that testifies to the large-scale control on the instability (i.e., the pattern is not set locally in the vicinity of the edge). This large-scale control is all the more conspicuous as one can see a couple of downwellings and upwellings that stretch across the whole block (Figure 17). Such pervasive structures were also observed in disk-shaped blocks. We found that the characteristic lengths and spacings of the convective structures that developed in square blocks do not differ significantly from those on disks, as shown in the various figures above.

3.5. Buoyancy Number

[39] We have carried out a few experiments to investigate the impact of the buoyancy number. This was only done for verification purposes as the influence of B had been

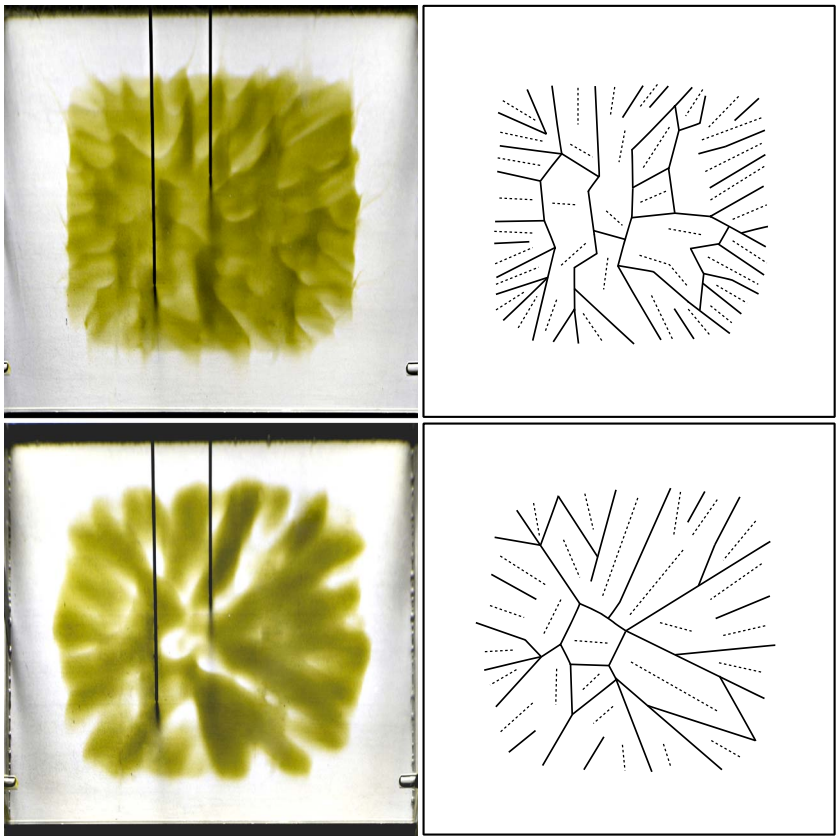

Figure 16. Experiment with a square-shaped unstable block (ASTICO 61, $Ra = 21$, $B = 0.22$, $h_d/R = 0.032$) at two different times ((top) $t = 4.6$, (bottom) $t = 22.3$). Note the marked radial structure and the coarsening of the pattern with time.

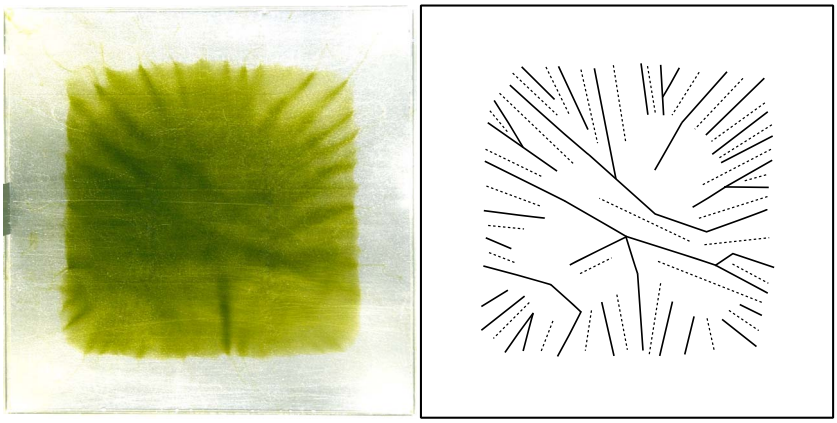

Figure 17. Experiment with a square-shaped block with a higher Rayleigh number than that of Figure 16 (ASTICO 77, $Ra = 74$, $B = 0.29$, $h_d/R = 0.033$) at $t = 1.5$. Note the radial pattern and the throughgoing structures.

comprehensively investigated in the layered configuration by *Jaupart et al.* [2007]. We checked that increasing the buoyancy number acts to increase the critical value of the Rayleigh number. This behavior has been assessed using 15 control experiments. We only show here the results of two end-member experiments with $B = 0.34$ and $B = 0.68$ (Figure 18). Both experiments are clearly located in the unstable domain for $B \sim 0.25$ and yet were unambiguously stable, with no interface deformation and no detectable temperature fluctuations. We also checked that the instability pattern is not sensitive to the buoyancy number in a 0.21–0.34 range.

3.6. Thickness Variations in the Unstable Block

[40] As discussed previously, the block was generated by letting dense and viscous fluid spread at the base of the tank. By construction, the block did not have a uniform thickness and thinned at the edges. This raises two questions on the experimental results and their applicability to Earth: Are the results sensitive to thickness variations and what is the amplitude of thickness variations in geological conditions? We address the former here and the latter in the following section.

[41] The very nature of the spreading implies that significant thickness variations are limited to a thin outer fringe whose width is a fixed fraction of the disk radius. We convinced ourselves that the experimental results are not sensitive to such thickness variations in two different ways. One critical fact is that the spatial pattern is determined at the scale of the whole block and not locally. This is clear from the large-scale arrangement of the structures but can also be ascertained using the characteristic dimensions of the convective structures. For example, the width of the outer annulus hosting the radial spoke pattern, s, is set by the overall aspect ratio of the disk independently of the size of the thinned fringe (Figure 12). Another observation is that the geometrical scalings are almost identical for squares and disks.

4. Instability of Continental Lithospheric Mantle: Conditions and Consequences

4.1. Geological Conditions

[42] We have drawn attention to the tiny values of the critical Rayleigh number at small values of the aspect ratio: these may be as small as 30, which emphasize the highly unstable nature of lithosphere stratification in this configuration. Here we briefly review the physical properties that must be specified to evaluate the instability potential of depleted continental lithosphere. Obtaining reliable estimates of the rheological properties of deep lithospheric mantle is a difficult exercise. If one uses laboratory data on mantle rocks, one must specify the water content and creep deformation mechanism as well as the potential temperature of the underlying asthenosphere. The uncertainty on the latter is frequently glossed over but is at least ±50 K, which alone is responsible for 1 order of magnitude uncertainty on viscosity [*Levy and Jaupart*, 2011]. If one seeks constraints from observations, one is left with very few studies. The characteristics of postseismic relaxation after large

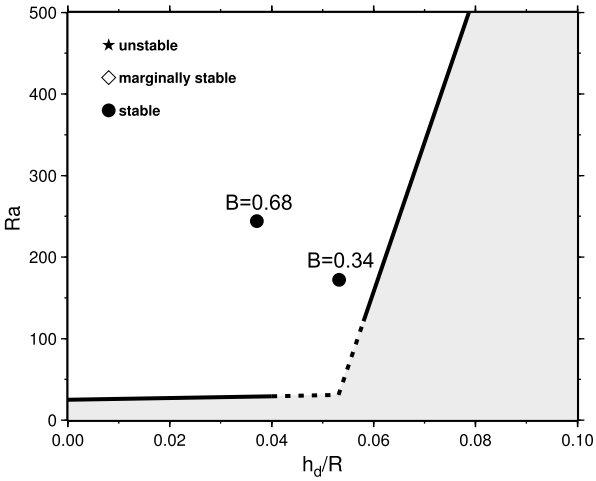

Figure 18. Experiments with higher buoyancy numbers (ASTICO 07 and ASTICO 26). The buoyancy number is given for each experiment and the stability line is the one determined for experiments with buoyancy numbers between 0.2 and 0.25. Both experiments are stable, illustrating that the critical Rayleigh number increases with the buoyancy number, as predicted by the theory and experiments of *Jaupart et al.* [2007].

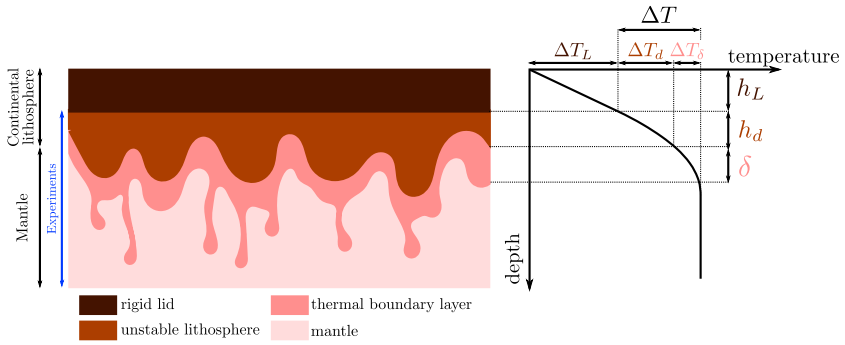

Figure 19. The two types of convection that occur in the experiments. The unstable lithosphere in light brown has a contorted base, with small-scale convection in dark pink still present in the asthenosphere below (light pink). The two forms of convection are associated with different wavelengths and characteristic times.

earthquakes indicate that the effective viscosities of both lithospheric and asthenospheric mantles may be as small as 10^{18} Pa·s [*Pollitz et al.*, 2000; *Freed et al.*, 2006]. Such determinations were obtained in active tectonic regions and may not be relevant to thick continental lithospheric roots, but they do show that the lithospheric mantle can deform on small time scales.

[43] As shown in *Jaupart et al.* [2007] and in section 2.1, the Rayleigh number of relevance here is not that for the convecting mantle but that for the potentially unstable depleted layer. Thus, the appropriate thickness (and length scale) is not the total depth of the Earth's mantle, but that of a sublayer of depleted mantle at the base of the lithosphere. In effect, we are studying the lithosphere independently of the larger-scale mantle circulation. In a calculation of *Ra*, one must allow for temperature-dependent viscosity and the fact that only part of the lithospheric mantle can become unstable, with an upper part that is too cold and too strong to get involved in convective motions. The characteristic temperature difference that determines viscosity variations has been called the "rheological" temperature difference ΔT_R and depends on an activation energy and an activation volume [*Davaille and Jaupart*, 1993; *Solomatov*, 1995]. The effective temperature difference across an actively convecting layer, noted ΔT_δ, is larger than this and depends on the exponent of the rheological law [*Solomatov and Moresi*, 2000; *Levy and Jaupart*, 2011]. This temperature difference is approximately such that viscosity varies by a factor 10 and takes values of 200 K or more for dislocation creep, which is the relevant deformation mechanism in upper mantle conditions [*Korenaga and Karato*, 2008; *Levy and Jaupart*, 2011]. As explained in *Jaupart et al.* [2007] and *Sleep and Jellinek* [2008], one must consider two boundary layers in the present problem (Figure 19). One, of thickness h_d, is that part of the lithospheric mantle that may become unstable and the other, of thickness δ, is the asthenospheric thermal boundary layer that lies below (Figure 19). The two boundary layers are responsible for two very different types of convective instability, as described above. They are identified in the experiments without ambiguity and both contribute to the total buoyancy driving convective motions. In such conditions, the temperature difference ΔT that enters both the Rayleigh and buoyancy numbers is the sum of contributions from the two boundary layers ($\equiv \Delta T_d + \Delta T_\delta \sim 2\Delta T_\delta$). We therefore estimate that ΔT may be equal to 400 K or more.

[44] To calculate the Rayleigh number, one must specify the value of h_d, which is the thickness of depleted lithospheric mantle that can become unstable. We have specified above the temperature difference across that part of the lithosphere, which is ΔT_d ($\sim \Delta T_\delta$), and can calculate the associated thickness as a function of the temperature gradient at the base of the lithosphere. This temperature gradient cannot be deduced from the total lithosphere thickness and mantle potential temperature because of the large amounts of heat producing elements that lie in continental crust. In addition, one must account for potentially nonnegligible heat production in the lithospheric mantle [*Michaut et al.*, 2007]. According to the extensive analysis of *Levy and Jaupart* [2011], the temperature gradient near the base of the lithosphere lies in a 3–5 K km^{-1} range. Thus, h_d lies in a 40–60 km range and we take $h_d = 50$ km. The density of the continental lithosphere can be determined from xenoliths and varies with age [*Poudjom Djomani et al.*, 2001], but an average value of 3300 kg·m^{-3} is accurate enough for the Rayleigh number calculation.

[45] At the relevant pressures and temperatures $\kappa = 7 \times 10^{-7}$ m^2·s^{-1}. As regards the coefficient of thermal expansion α, we refer to the analysis by *Schutt and Lesher* [2006], who found that it is significantly larger than previous estimates in the (P,T) conditions of lithospheric roots and may be as large as 5×10^{-5} K^{-1}. Using $\alpha = 4.5 \times 10^{-5}$ K^{-1}, it would take viscosities of 10^{22} Pa·s or more for the Rayleigh number of the "rheological" sublayer of lithospheric mantle to be subcritical. For example, this Rayleigh number is $\approx 10^2$ for a viscosity of 10^{21} Pa·s.

[46] Estimating the buoyancy number is also difficult, due to the lack of reliable data on the intrinsic density of lithospheric mantle at the large scale that is required here. Using measurements on xenoliths suites, *Poudjom Djomani et al.* [2001] have suggested that this density decreases with increasing stabilization age for the continent due to systematic changes of chemical depletion. For Proterozoic lithosphere, they estimated an intrinsic buoyancy in a 15–30 kg·m^{-3} range. *Schutt and Lesher* [2006] have recently compiled a comprehensive data set on the physical properties of mantle minerals and on chemical depletion effects due to melting. They estimate that in the (P,T) conditions that prevail below 200 km depth, 10% melt depletion in mantle material is equivalent in density impact to a 30–60 K increase in temperature, depending on pressure.

Table 3. Characteristic Dimensions and Spacings for Intracratonic Basins, Volcanic Swells, and Basins

Continent	Rifts	Age	Length (km)	Reference
N. America	Marathon and Reelfoot	Ordovician (≈ 450 Myr)	500–600	*Thomas* [2011]
N. America	Southern Oklahoma	Ordovician (≈ 450 Myr)	1000	*Keller and Baldridge* [2006]
Australia	Adelaide	Neoproterozoic (≈ 840 Myr)	700	*de Vries et al*. [2008]
W. Africa	Cameroon Volcanic Line	Cenozoic (65 Myr to present)	1000	*Guiraud et al*. [2005]
	Basins or Swells	Age	Distance (km)	Reference
N. America	four basins Illinois, Michigan, Williston, Hudson Bay	Ordovician (≈ 450 Myr)	800–1500	*Allen and Armitage* [2012]
N. America	three domal uplifts Ozark, Nashville, Cincinnati	Ordovician (≈ 450 Myr)	500–700	*Allen and Armitage* [2012]
Australia	four basins Officer, Amadeus, Georgina and Ngalia	Neoproterozoic (≈ 840 Myr)	500–800	*de Vries et al*. [2008]
W. Africa	multiple domal uplifts; see Figure 2	Cenozoic (65 Myr to present)	400–1000	*Guiraud et al*. [2005]

These results emphasize that near the base of the lithosphere, it does not take large temperature differences to balance the effect of depletion. For a total driving temperature difference $\Delta T = 400$ K, as explained above, $\alpha = 4.5 \times 10^{-5}$ K^{-1} and $\rho = 3.3 \times 10^3$ kg·m^{-3}, we find that $\Delta\rho_T \approx 60$ kg·m^{-3}. Thus, using the density estimates of *Poudjom Djomani et al*. [2001], the buoyancy number of Proterozoic lithosphere may be as small as 0.25, as in the experiments of this paper. For Archean cratonic lithospheric roots, the intrinsic buoyancy is larger and possibly as large as 45 kg m^{-3} [*Doin et al*., 1996]. In this case, the buoyancy number is expected to be larger than 0.5, which does not allow for the instabilities studied in this paper.

[47] The above arguments illustrate current difficulties in accurately assessing dynamic conditions near the base of subcontinental lithospheric mantle. They do show, however, that thermally driven negative buoyancy is largest in the lower reaches of continental roots due to enhanced thermal expansion and that the lithospheric mantle is close to the instability threshold.

4.2. Formation of Rifts and Domal Uplifts

4.2.1. Geometrical Characteristics

[48] We recapitulate the main features of the instability and estimate the relevant length scales for continental lithosphere. In a homogeneous continent, the instability manifests itself as a continent-wide phenomenon with different characteristics near the edge and in the interior. Near the edge of the continent, instability proceeds as a set of linear radially oriented downwellings and upwellings that grow at a right angle to the boundary. Above an upwelling between two downwellings, the lithosphere is put in tension due to the diverging flow. The expected geological consequence of this is a rift that strikes at a right angle to the continent-ocean boundary. In the interior region, instability proceeds through polygonal cells with domal uplifts that are organized in a quasiperiodic array. The model predicts that these structures should appear at specific times: Lithosphere instabilities should develop following continental breakup or accretion due to the induced changes of continental size and shape. We now specify the dimensions and spacings of the geological structures that should be induced.

[49] For $h_d \approx 50$ km, as estimated above, the vertices of the polygonal cells lie at distances of about 300 km and the centers of two adjacent cells are about 500 km apart (see section 3.2). As discussed above and illustrated in Figure 13, these distances are larger when the size of the unstable block cannot accommodate a large number of cells, which is the case of continents. With time, the pattern evolves and coarsens slowly, such that these distances increase (Figure 15). For the geological timescales of interest here, such variations are small, however. In conclusion, full-fledged surface consequences of the convective planform that develops at the base of the lithosphere are expected to be separated by distances that exceed 500 km. We can also predict the length of rifts at the edges of continents, which we attribute to the linear upwellings that develop in an outer fringe of width s. Following equation (5), one must specify the aspect ratio of the continental block. Allowing for the fact that Archean cratons are likely to remain stable, we focus on blocks of Proterozoic or younger ages. For Africa, the lateral extent of the Proterozoic-Phanerozoic basement domain is about 3000 km, so that $R \approx 1500$ km and hence $h_d/R \approx 0.03$. We deduce that $s/R \approx 0.70$ and hence $s \approx 1000$ km. Such distances are close to those of many continental rifts (Table 3). The key point in this discussion is perhaps that the instability develops over distances that are much larger than the thickness of the layer that goes unstable; thus, even a thin sublayer at the base of the lithosphere can generate structures that are separated by geologically relevant distances.

[50] These results rely on the assumption of a homogeneous continent with a simple overall shape such as a disk or a square. They must be considered as order-of-magnitude estimates and can only be applied to real continents with due care for the inevitable complexities that arise in nature. In practice, one should account for the fact that a continent is not homogeneous and has been assembled out of units with different ages and compositions. Highly depleted lithospheric mantle beneath Archean cratons, for example, is not likely to become unstable. In this regard, it is striking that the current active features of western Africa clearly avoid the Archean cratons and are confined to provinces of younger ages (Figure 2), which is consistent with the likely values of B in Archean lithosphere.

4.2.2. Impact of Destabilization on the Lithospheric Lid

[51] Convective breakdown of the basal part of the lithosphere generates upwellings that exert a diverging strain field and bring hot asthenosphere in contact with the stable upper part of the lithosphere (or "lid"), which promotes extension and uplift. We now assess whether the flow can induce the geological structures that are observed at Earth's surface. It is worth remembering that we are not dealing with full-fledged rifting leading to major crustal disruption and seafloor spreading, but rather with "failed" rifts. Indeed, one of the most remarkable features of intracontinental rifts, swells, and basins, as well as the Cameroon line, is the lack of significant crustal thinning. For example, in the central United States, the Moho depth does not vary along the 400 km

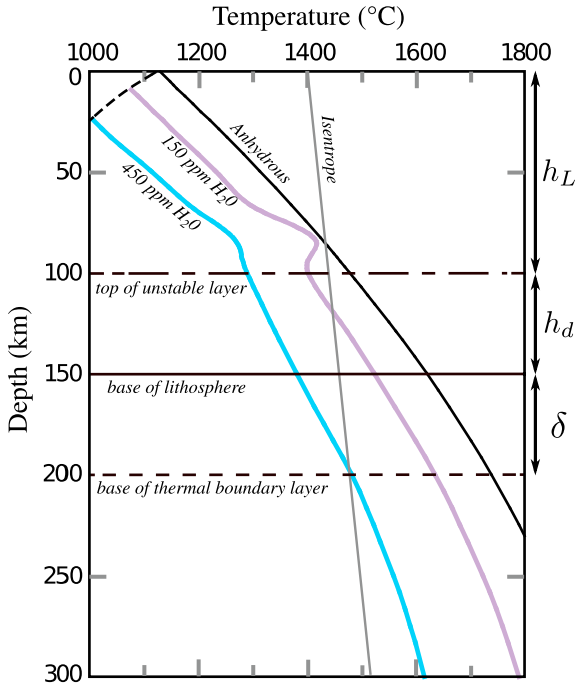

Figure 20. Schematic structure of an unstable continental lithosphere with peridotite solidus curves from *Hirschmann et al.* [2009]. Thick black line: anhydrous solidus. Purple and blue lines: solidi for water concentrations of 150 and 450 ppm, respectively. The thin grey line is a mantle adiabat for a potential temperature of 1400°C with a slope of 13 K·GPa^{-1}. For a water concentration as low as 150 ppm, partial melting occurs at depths of 120 km or less as convective breakdown of the lithospheric mantle brings asthenosphere up.

south-to-north seismic profile that crosses the Reelfoot rift and reaches into the Illinois basin [*Catchings*, 1999]. There is only a very modest (≈2 km) change of crustal thickness beneath the southern Oklahoma aulacogen and it is a thickness increase [*Keller and Baldridge*, 2006]. This is also true for the Williston basin, below which no significant crustal thinning can be detected [*Morel-à-l'Huissier et al.*, 1987; *Nelson et al.*, 1993]. Indeed, *Nelson et al.* [1993] state that the geophysical evidence "militates against the idea that crustal stretching played a significant role in the formation of the basin." The Cameroon Volcanic Line is not associated with any changes of crustal thickness either [*Tokam et al.*, 2010]. The observations, therefore, indicate that little if not zero bulk extension has occurred beneath all these structures.

[52] The failed rifts and swells of continental interiors cannot be attributed to the forces that drive plate motions and large-scale continental deformation, such as slab pull and ridge push. Slab pull can be ruled out, for example, because these geological structures appeared following continental breakup with no active subduction in the vicinity. Ridge push is active in their cases, but it is not clear how it can generate both rifts and swells, and in particular rifts or volcanic "lines" with such orientations to the direction of oceanic expansion. This is well illustrated by western Africa today. Mantle plumes can also be ruled out, at least in the case of western Africa, as shown in section 1.

[53] In section B, we calculate the net force that is generated by the instability of a basal lithospheric layer and obtain 0.81 TN·m^{-1} (TN = 10^{12} N). This is slightly smaller than, but comparable to, slab pull and ridge push. These two forces are due to the negative buoyancy of cold oceanic plates and elevation of oceanic ridges, respectively. The former force increases with increasing length of the subducting slab [*Carlson et al.*, 1983; *Lallemand et al.*, 2005]. In a downgoing slab, a large part of the gravity pull is balanced by friction, so that the net force exerted on the surface plate is much smaller than the nominal buoyancy force. According to *Copley et al.* [2010], the net driving force exerted on the Indian plate by slab pull is ≈2.5 TN·m^{-1}. The ridge push force increases linearly with sea floor age until about 40 Myr and levels off at a value of about 3 TN·m^{-1} [*Forsyth and Uyeda*, 1975; *Parsons and Richter*, 1980; *Bott*, 1989]. It is partly balanced by viscous shear at the base of the lithosphere [*Carlson et al.*, 1983]. *Copley et al.* [2010] estimate that the net force that is applied to the Indian plate is again 2.5 TN·m^{-1}, just like slab pull. Thus, the force that is associated with the convective breakdown of the lithospheric mantle (≈ 0.8 TN·m^{-1}) is only three times smaller than the forces which are responsible for the rise and support of the Himalayas.

[54] We face the same basic problem as for all physical models of continental extension because the force available is much less than the integrated strength of the lithosphere in areas of "normal" heat flow [*Hopper and Buck*, 1993]. Most such models do not address this difficulty because they are kinematic ones with extension rates that are imposed. In a recent review, *Buck* [2004] has advocated two types of effects that may explain why extension and rifting do occur. One is that if grain sizes in the lithospheric mantle are small enough, deformation may proceed by diffusion creep, albeit at small rates. The other, and most likely one, is that multiple intrusion of basaltic dykes weaken the lithosphere both thermally and mechanically, through the fluid pressure that is exerted on the lithospheric mantle. With our mechanism, destabilization of the lower part of the lithosphere induces upwelling of the asthenospheric mantle. Figure 20 shows liquidus curves for anhydrous and weakly hydrated asthenosphere. We adopt values for mantle temperature and lithospheric thickness from *Levy and Jaupart* [2011], which are consistent with heat flow data and seismological tomographic models in northern America. We use the same parameters and physical properties as above. We consider a nominal depleted lithosphere that is 150 km thick with a 50 km thick thermal boundary layer, such that the "thermal" lithosphere, which encompasses both, is 200 km thick, which is appropriate for Proterozoic lithosphere [*McKenzie and Priestley*, 2008; *Levy and Jaupart*, 2011]. In this case, convective breakdown, which involves the asthenospheric thermal boundary layer and the lower part of the depleted lithospheric mantle (Figure 19), affects a total vertical extent of 100 km and brings asthenospheric material from ≈200 km depth to ≈100 km. We take a mantle potential temperature of 1400°C, which is consistent with the lithosphere thickness chosen [*Levy and Jaupart*, 2011]. One last parameter that must be specified is the water content of asthenospheric mantle, which we take to be in a 150–450 ppm range following *Bell and Rossman* [1992], *Saal et al.* [2002], *Peslier and Luhr* [2006], and *Till et al.* [2010]. Figure 20 shows that partial melting occurs for this choice of parameters. A smaller

potential temperature would be associated with thinner lithosphere, but destabilization would involve the same total thickness of ≈100 km and would bring asthenospheric material at lower pressures, which would enhance the likelihood of partial melting. Partial melting can be prevented if the following conditions are met: a lithosphere that is much thicker than 200 km, a mantle potential temperature that is less than 1350°C or a dry asthenosphere. As regards mantle temperature, recent determinations support values in excess of 1400°C [*Putirka*, 2008]. Lithosphere that is thicker than 200 km seems confined to Archean domains, and there seems to be little doubt that the asthenosphere is not dry. We thus conclude that the convective breakdown of the lower part of the lithospheric mantle is indeed likely to induce partial melting and volcanism.

[55] We conclude that our mechanism meets several key requirements. It generates the right kind of stress field at the base of the stable lid as well as melting in the asthenosphere that is rising beneath it, which induces weakening of the lithospheric mantle. It exerts forces on the lithosphere that are not very different than those of large-scale mantle convection. Finally, it acts at the relevant spatial scales and, in particular, provides one explanation for the length of failed continental rifts.

4.2.3. Implications: Continental Breakup and Instability

[56] This study shows that the dimensions and shape of the continent affect both the likelihood of instability and the dimensions of the convective structures that develop, which has several consequences. One is that changes of continental size, due to breakup or amalgamation, are likely to induce new instability patterns and geological activity. By construction, such activity affects whole continents in a restricted time interval in relation to large-scale plate reorganizations. We have briefly reviewed evidence for contemporaneous events in the section 1 and the important point is that these occur following major continental rearrangements. Previous authors have noted that the formation of intracratonic basins occurs at very specific times, most commonly following continental dispersal [*Klein and Hsui*, 1987; *Allen and Armitage*, 2012]. For example, the basins of Africa and North and South America are linked to the breakup of Rodinia, Gondwana, and Pangaea. This has been attributed to the large-scale geodynamic regime and induced plate-wide tectonic stress distribution [*Allen and Armitage*, 2012] but no physical model has been developed to elaborate on this hypothesis. According to this paper, the answer lies in the intrinsic dynamics of the continental lithospheric root. Each part of the broken supercontinent rearranges its basal convection pattern during dispersal without large-scale coordination from the convecting mantle.

4.2.4. Discussion

[57] Starting from a flat initial configuration, destabilization of the lithospheric mantle induces large undulations of the lithosphere-asthenosphere interface. Preexisting variations of lithosphere thickness can induce mantle flows and could prevent this type of instability if they occur on the same scale. We know that the thickness of continental lithosphere changes across a continent in relation to age and tectonic amalgamation events [*Shapiro et al*., 2004; *McKenzie and Priestley*, 2008; *Levy and Jaupart*, 2011]. Such changes follow a global pattern that is on a much larger scale than the distances advocated here. Current seismic maps reveal large areas with no significant variations of lithosphere thickness. In Africa, for example, thickness variations seem limited to a few deep keels that are associated with Archean provinces [*McKenzie and Priestley*, 2008] away from the spectacular network of active rifts and volcanic centers.

[58] The critical Rayleigh number for instability is very small at small values of the aspect ratio and increases sharply as the aspect ratio becomes larger than 0.05. From our discussion on the Rayleigh number, it appears that it probably does not take values larger than 10^3 or so. Thus, the aspect ratio of 0.05 may be regarded as a critical threshold for the instability. As discussed above, thickness h_d corresponds to that part of the lithospheric mantle, which can become unstable, and is estimated to be about 50 km. From this, we deduce a critical continental radius of about 1000 km, below which instability is prevented. This is approximately the half-width of the smallest unstable continental domain, which we identify with the Proterozoic to Phanerozoic part of the smallest continent of today, Australia. Smaller continental blocks that may have been independent landmasses early in Earth's history, such as the Archean Yilgarn and Pilbara cratons of western Australia, were probably sufficiently small to remain unaffected by the type of instabilities that we have described in this paper. It takes relatively large continents such as the present-day ones to allow the convective breakdown of continental lithosphere.

[59] We have discussed above viscosity values for the lower part of the lithospheric mantle, which depend on a host of parameters and temperature in the well-mixed asthenosphere. This viscosity value sets the Rayleigh number for the potentially unstable rheological sublayer of depleted mantle as well as the periodicity for instabilities, which is [*Jaupart et al*., 2007]

$$\tau = \frac{2\pi}{\omega'_c}\frac{\eta_1}{\rho_0 \alpha \Delta T g h_d}, \tag{6}$$

where ω'_c is the critical dimensionless frequency, equal to $\sim 50\times10^{-4}$ for $B \sim 0.25$. Using $\alpha = 4.5 \times 10^{-5}\mathrm{K}^{-1}$, $h_d = 50$km, ΔT = 400 K and viscosity in a $10^{20}-10^{21}$ Pa·s range, τ is between 100 Myr and 1 Gyr. This timescale corresponds to the time between two instability cycles, which is twice as long as the duration of the waxing phase of each cycle. In the experiments, we have found that successive instabilities eventually lead to mixing of the block with the ambient fluid. One could infer from this that the lithospheric mantle should ultimately disappear, which would not be consistent with the geological record. Two factors prevent such an evolution, however. One is that only a small number of instabilities are allowed with the same continental configuration. The Wilson cycle of break-up and collision proceeds on a timescale of a few hundreds of millions of years [*Wilson*, 1966; *Allegre and Jaupart*, 1985], implying that few lithospheric oscillations are allowed before large-scale reorganization occurs. Another factor is that the instability process acts to modify the composition and rheological properties of the lithospheric mantle that goes unstable. Such material gets heated as it sinks into the asthenosphere and then undergoes pressure release as it rises back up. This should lead to decompression melting and hence strengthening, which would act to weaken the next instability.

[60] Convective breakdown of the rheological sublayer induces thinning and thickening in different parts of the depleted lithospheric mantle, which in turn induce large-scale lateral variations of heat supply to the stable lithospheric lid. Such changes of heat supply could be reflected in surface heat flow anomalies provided that the convective pattern remains steady for a time that is longer than the characteristic time for diffusion across the lid. According to the analysis above, the lid is expected to be about 100 km thick, and the diffusion timescale ($h_L^2/(4\kappa)$) is 110 Myr, which is within the range of timescales for the instability. If we consider the Cameroon case, where magmatic and volcanic activity began 70 Myr ago [*Déruelle et al.*, 1991], we expect local heat flow anomalies associated with recent crustal intrusions but no larger-scale anomaly due to the deeper convective breakdown process.

5. Conclusion

[61] We have documented in detail the characteristics of convective instabilities that may affect chemically depleted continental lithosphere. One key result is that a thin sublayer at the base of the lithosphere can generate structures that are separated by geologically relevant distances in a 500–1000 km range. Our study emphasizes the large-scale lithospheric control on the instability and the continent-wide pattern that is expected to develop within a small time interval following continental breakup. It also illustrates how rifts that develop at the edge of a continent can be linked in both space and time to scattered volcanic activity or basin formation occurring in the continents interior. Finally, it shows that the shape and size of the continent play important roles and must be accounted for when comparing different continents. Further studies must be made to evaluate such subtle geometrical controls. According to this study, an important control on continental events is the intrinsic buoyancy of lithospheric mantle. The same statement is valid for mantle plume-induced perturbations [*Jurine et al.*, 2005]. This is one way in which the large-scale fabric of a continent manifests itself, through the juxtaposition of provinces with different ages, compositions, and hence intrinsic buoyancies.

Appendix A: Spreading of the Unstable Block

[62] One critical aspect of the laboratory setup was to ensure that the disk did not spread significantly over the time of an experiment (typically 60 min). For a fixed volume, *Huppert* [1982] showed theoretically that the shape of a spreading dome is

$$H = \left(1 - \xi^2\right)^{1/3}, \tag{A1}$$

where H is the dimensionless thickness (scaled to the maximum axial value) and ξ is the dimensionless radial distance (scaled to the dome radius). Figure A1 compares the shape of our experimental disk (black circles) with theory right before heating starts for two distinct experiments. The disks' viscosities varied over 1 order of magnitude. The shapes of the experimental disks are close to theoretical expectations and very close to one another. They can be described by an expression of the form $H=(1-\xi^2)^{1/n}$ with an exponent between 1/2 and 1/3.

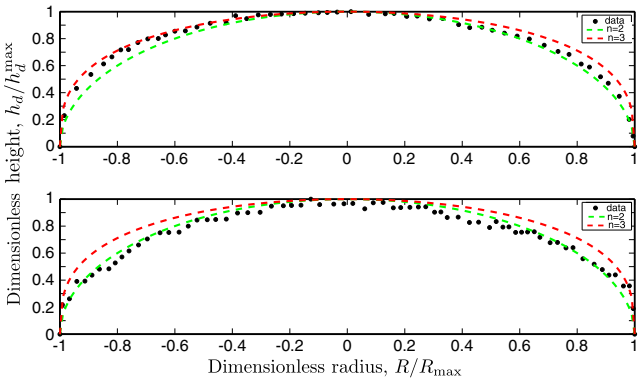

Figure A1. Vertical cross sections through the disks in two different experiments just before heating. The green and red dashed lines are the theoretical shapes from equation (A1) with $n=2$ and $n=3$, respectively. We show experiments (top) `ASTICO 40` ($Ra = 59$, $B = 0.25$, $h_d/R = 0.055$) and (bottom) `ASTICO 45` ($Ra = 103$, $B = 0.22$, $h_d/R = 0.028$).

[63] The experiments do not conform exactly to equation (A1) because the fluid was not left to spread for sufficiently long. In other words, the shape was still influenced by the injection phase and was not in its asymptotic form yet. We verified that it did tend toward the asymptotic prediction by tracking how the best fit exponent evolved with time.

[64] The dense fluid was spreading at negligible rates in the course of an experiment, as can be easily verified by comparing the initial and final radii. Thus, heat transport within the block was achieved by conduction before the onset of instability. This can be ascertained quantitatively using the Peclet number, $Pe=h_dU/\kappa$, where U is the horizontal spreading velocity and κ thermal diffusivity. The decreasing values of block thickness and spreading rate rapidly lead to small values of the Peclet number, typically of order 10^{-1}. Thus, horizontal heat advection plays a negligible role in the experiments.

Appendix B: Force Exerted on the Lithospheric Lid

[65] We estimate the force that is applied by the convective flow on the lithospheric lid that remains stable due to its cold temperatures and high mechanical strength. We consider fully developed flow such that the amplitude of the deformation is equal to the thickness of the unstable layer, as illustrated in Figure B1. In these conditions, downwellings act to thin the unstable layer to zero thickness, and upwellings proceed to the base of the stable lid. These conditions are illustrated in the laboratory experiments of Figure 6B or Figure 14, for example. The flow is driven by the negative buoyancy due to the cold temperatures and proceeds at a rate that is faster than that of thermal diffusion [*Jaupart et al.*, 2007]. In this case, the asthenospheric thermal boundary layer follows the general deformation. The unit made of the layer of intrinsically buoyant material and underlying thermal boundary layer has initial thickness $h_o=h_{do}+\delta_o$, where h_{do} and δ_o are the initial thicknesses of the sublayer of

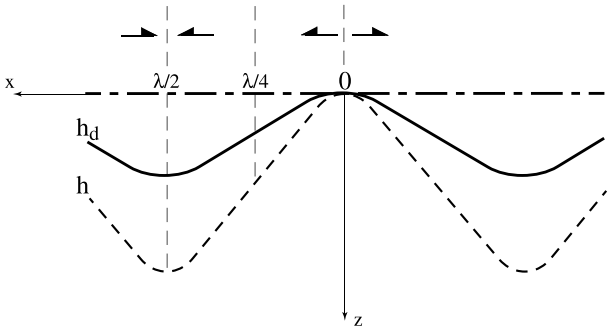

Figure B1. Diagram showing the unstable lower part of the lithospheric mantle and the distorted asthenospheric thermal boundary layer. $z=0$ is at the top of the unstable layer (and at the base of the stable lid), the thick line is the deformed lower surface of the depleted lithosphere ($z = h_d$), the thick dotted line is the base of the asthenospheric thermal boundary layer ($z = h_d + \delta = h$). Arrows denote regions in extension ($x=0$) and compression ($x = \lambda/2$).

buoyant material and basal thermal boundary layer, respectively. This unit gets distorted such that its thickness h is given by

$$h = h_o\left(1 + \sin\left[2\pi\frac{x}{\lambda}\right]\right). \tag{B1}$$

[66] We further assume that both layers have been affected by the same geometrical transformation, such that the thickness of the deformed depleted material, for example, is

$$h_d = h_{do}\left(1 + \sin\left[2\pi\frac{x}{\lambda}\right]\right). \tag{B2}$$

[67] We shall see that the stresses that are generated by the instability can be calculated independently of the specific forms for the interface displacements and they are given here for simplicity and convenience. The density is such that

$$\text{for } 0 \le z \le h_d, \quad \rho = \rho_o\left(1 - \frac{\Delta\rho_c}{\rho_o} - \alpha[T - T_o]\right); \tag{B3}$$

$$\text{for } h_d < z \le h, \quad \rho = \rho_o(1 - \alpha[T - T_o]); \tag{B4}$$

$$\text{for } z > h, \quad \rho = \rho_o; \tag{B5}$$

where the intrinsic density contrast due to depletion, $\Delta\rho_c$, is positive and T_o is the temperature of the well-mixed bulk fluid. Neglecting diffusion, the temperature profile is as follows:

$$T(z) = T_o + \Delta T\left(\frac{z}{h} - 1\right), \tag{B6}$$

where ΔT is the total temperature difference across the unstable region (see text above). For the large wavelengths and the rather small thicknesses involved here, one can write the momentum equations in the lubrication approximation:

$$0 = -\frac{\partial P}{\partial x} - \frac{\partial \tau_{zx}}{\partial z}, \tag{B7}$$

$$0 = -\frac{\partial P}{\partial z} + \rho g, \tag{B8}$$

where τ_{zx} is the horizontal shear stress and where we have used the sign convention that stresses are acting on material that lies on the positive side of a surface. It is convenient to introduce the hydrostatic pressure field P_o in a homogeneous medium of density ρ_o and "dynamic" pressure $p = P - P_o$. At the base of the unstable layer, at $z = h$, one has $p(h) = 0$. Using this pressure, the body force term in the vertical momentum equation involves the density anomaly $\rho - \rho_o$. From equation (B8), we find that

$$\int_z^h \frac{\partial p}{\partial z}\mathrm{d}z = p(h) - p(z) = -p(z) \quad \text{for } z > h, \tag{B9}$$

$$= -\alpha\rho_o g\Delta T\left(-\frac{h}{2} + z - \frac{z^2}{2h}\right) \quad \text{for } h_d < z \le h, \tag{B10}$$

$$= -\Delta\rho_c g(h_d - z) - \alpha\rho_o g\Delta T\left(-\frac{h}{2} + z - \frac{z^2}{2h}\right) \quad \text{for } 0 \le z \le h_d, \tag{B11}$$

which specifies the "dynamic" pressure field. Turning to equation (B7), we find that

$$\tau_{zx}(\mathrm{x},0) = \int_0^h \frac{\partial p}{\partial x}\mathrm{d}z \tag{B12}$$

$$= \Delta\rho_c g h_d \frac{\partial h_d}{\partial x} - \frac{1}{3}\alpha\rho_o\Delta T g h\frac{\partial h}{\partial x}, \tag{B13}$$

where we have assumed that the shear stress vanishes at $z = h$, which is appropriate for this particular flow. In geological reality, there may be some regional stress due to large-scale mantle flow, but this is outside the scope of this model. We now calculate the forces that are applied to the stable lid, which can be split in alternating zones of tension and compression, as illustrated in Figure B1. We separate these zones by vertical surfaces, at $x = x_1$ and $x = x_2$, say, so that we can write the dynamical equilibrium of a lithospheric block of width $x_2 - x_1$ in the horizontal direction as follows:

$$F_1 + F_2 - \int_{x_1}^{x_2} \tau_{xz}\mathrm{d}x = 0, \tag{B14}$$

where F_1 and F_2 are the horizontal forces that act on the vertical sides of the block and where we have accounted for the fact that the block lies on the negative side of the $z=0$ surface. Vertical surfaces at $x_1 = 0$ and $x_2 = \lambda/4$ encapsulate a block in tension such that $F_2 = 0$, as x_2 marks the transition to the adjacent block in compression (Figure B1). Thus,

$$F_1 = \int_0^{\lambda/4} \tau_{xz}\mathrm{d}x \tag{B15}$$

$$= \frac{1}{2}\Delta\rho_c g\, h_d^2\big|_{x=\lambda/4} - \frac{1}{6}\alpha\rho_o g\Delta T\, h^2\big|_{x=\lambda/4} \tag{B16}$$

[68] This force is negative because it balances the basal shear that is exerted by the flow in the positive x direction.

[69] From equations for h_d and h, $h_d|_{x=\lambda/4} = h_{do}$ and $h|_{x=\lambda/4} = h_o$. Using values for the various variables from the main text, $h_{do} \approx 50$ km, $h_o \approx 100$ km, $\Delta\rho_c = 15$ kg·m^{-3}

and $\Delta\rho_T = 60$ kg·m^{-3}, we find that the magnitude of $F_1 = 0.81$ TN·m^{-1} (TN = 10^{12} N). For comparison, the net forces exerted on the Indian plate by subduction zones and the Indian mid-ocean ridge are both ≈2.5 TN·m^{-1} [*Copley et al.*, 2010].

[70] **Acknowledgments.** We thank the Associate Editor, Ctirad Matyska, and two anonymous reviewers for their useful comments, criticisms, and suggestions which greatly helped us improve the manuscript.

References

Allegre, C. J., and C. Jaupart (1985), Continental tectonics and continental kinetics, *Earth Planet. Sci. Lett.*, *74*, 171–186, doi:10.1016/0012-821X(85)90020-2.

Allen, P. A., and J. J. Armitage (2012), Cratonic basins, in *Tectonics of Sedimentary Basins: Recent Advances*, edited by C. Busby, and A. Azor, pp. 602–620, John Wiley & Sons, Chichester, U.K., doi:10.1002/9781444347166.ch30.

Bell, D. R., and G. R. Rossman (1992), Water in Earth's mantle—The role of nominally anhydrous minerals, *Science*, *255*, 1391–1397, doi:10.1126/science.255.5050.1391.

Bosworth, W., and C. K. Morley (1994), Structural and stratigraphic evolution of the Anza rift, Kenya, *Tectonophysics*, *236*, 93–115.

Bott, M. (1989), Plate boundary forces at subduction zones and trench-arc compression, *Tectonophysics*, *170*, 1–15, doi:10.1016/0040-1951(89)90099-1.

Buck, W. (2004), Consequences of asthenospheric variability on continental rifting, in *Rheology and Deformation of the Lithosphere at Continental Margins*, edited by G. D. Karner, B. Taylor, N. W. Driscoll, and D. L. Kohlstedt, Margins Theoretical and Experimental Earth Science Series, pp. 1–30, Natl Sci Fdn, Meeting on Rheology and Deformation of the Lithosphere at Continental Margins, US MARGINS Theoret & Experiment Inst, Snowbird, UT, JAN 23–26, 2000.

Carlson, R. L., T. W. C. Hilde, and S. Uyeda (1983), The driving mechanism of plate tectonics: Relation to age of the lithosphere at trenches, *Geophys. Res. Lett.*, *10*, 297–300, doi:10.1029/GL010i004p00297.

Catchings, R. (1999), Regional Vp, Vs, Vp/Vs, and Poisson's ratio across Earthquake Source Zones from Memphis, Tennessee, to St. Louis, Missouri, *Bull. Seism. Soc. Am.*, *89*, 1591–1605.

Charlson, G., and R. Sani (1970), Thermoconvective instability in a bounded cylindrical fluid layer, *Int. J. Heat Mass Tran.*, *13*(9), 1479–1496, doi:10.1016/0017-9310(70)90181-X.

Charlson, G., and R. Sani (1971), On thermoconvective instability in a bounded cylindrical fluid layer, *Int. J. Heat Mass Tran.*, *14*(12), 2157–2160, doi:10.1016/0017-9310(71)90037-8.

Copley, A., J.-P. Avouac, and J.-Y. Royer (2010), India-Asia collision and the Cenozoic slowdown of the Indian plate: Implications for the forces driving plate motions, *J. Geophys. Res.*, *115*, B03410, doi:10.1029/2009JB006634.

Croquette, V., M. Mory, and F. Schosseler (1983), Rayleigh-Bénard convective structures in a cylindrical container, *J. Phys. Paris*, *44*, 293–301.

Davaille, A., and C. Jaupart (1993), Transient high-Rayleigh-number thermal convection with large viscosity variations, *J. Fluid Mech.*, *253*, 141–166, doi:10.1017/S0022112093001740.

Déruelle, B., C. Moreau, C. Nkoumbou, R. Kambou, J. Lissom, E. Njongfang, R. T. Ghogomu, and A. Nono (1991), Chap. 9: The Cameroon Line: A review, in *Magmatism in Extensional Structural Settings*. *The Phanerozoic African Plate*, Springer-Verlag, Berlin, pp. 274–327.

Doin, M.-P., L. Fleitout, and D. McKenzie (1996), Geoid anomalies and the structure of continental and oceanic lithospheres, *J. Geophys. Res.*, *101*, 16,119–16,136.

Ebinger, C. J., and N. H. Sleep (1998), Cenozoic magmatism throughout east Africa resulting from impact of a single plume, *Nature*, *395*, 788–791, doi:10.1038/27417.

Farrington, R. J., D. R. Stegman, L. N. Moresi, M. Sandiford, and D. A. May (2010), Interactions of 3D mantle flow and continental lithosphere near passive margins, *Tectonophysics*, *483*, 20–28, doi:10.1016/j.tecto.2009.10.008.

Forsyth, D. W., and S. Uyeda (1975), On the relative importance of the driving forces of plate motions, *Geophys. J. R. Astron. Soc.*, *43*, 163–200, doi:10.1111/j.1365-246X.1975.tb00631.x.

Freed, A. M., R. Bürgmann, E. Calais, J. Freymueller, and S. Hreinsdóttir (2006), Implications of deformation following the 2002 Denali, Alaska, earthquake for postseismic relaxation processes and lithospheric rheology, *J. Geophys. Res.*, *111*, B01401, doi:10.1029/2005JB003894.

Furman, B., J. Bryce, T. Rooney, B. Hanan, G. Yirgu, and D. Ayalew (2006), Heads and tails: 30 million years of the afar plume, in *The Structure and Evolution of the East African Rift system in the Afar Volcanic Province*, vol. 259, edited by G. Yirgu, C. Ebinger, and E. P. K. H. McGuire, pp. 97–121, Geological Society of London Spec. Publ., London, U.K., doi:10.1144/GSL.SP.2006.259.01.09.

Gallacher, R. J., and I. D. Bastow (2012), The development of magmatism along the Cameroon Volcanic Line: Evidence from teleseismic receiver functions, *Tectonics*, *31*, TC3018, doi:10.1029/2011TC003028.

Garnero, E. J., and A. K. McNamara (2008), Structure and dynamics of Earth's lower mantle, *Science*, *320*, 626–628, doi:10.1126/science.1148028.

Guiraud, R., W. Bosworth, J. Thierry, and A. Delplanque (2005), Phanerozoic geological evolution of Northern and Central Africa: An overview, *J. African Earth Sci.*, *43*, 83–143, doi:10.1016/j.jafrearsci.2005.07.017.

Hirschmann, M. M., T. Tenner, C. Aubaud, and A. C. Withers (2009), Dehydration melting of nominally anhydrous mantle: The primacy of partitioning, *Phys. Earth Planet. In.*, *176*, 54–68, doi:10.1016/j.pepi.2009.04.001.

Hopper, J. R., and W. R. Buck (1993), The initiation of rifting at constant tectonic force - Role of diffusion creep, *J. Geophys. Res.*, *98*, 16213, doi:10.1029/93JB01725.

Huppert, H. E. (1982), The propagation of two-dimensional and axisymmetric viscous gravity currents over a rigid horizontal surface, *J. Fluid Mech.*, *121*, 43–58.

Jaupart, C., P. Molnar, and E. Cottrell (2007), Instability of a chemically dense layer heated from below and overlain by a deep less viscous fluid, *J. Fluid Mech.*, *572*, 433–469, doi:10.1017/S0022112006003521.

Jurine, D., C. Jaupart, G. Brandeis, and P. J. Tackley (2005), Penetration of mantle plumes through depleted lithosphere, *J. Geophys. Res.*, *110*, B10104, doi:10.1029/2005JB003751.

Keller, G., and W. Baldridge (2006), Chapter 12 the southern Oklahoma aulacogen, in *Continental Rifts: Evolution, Structure, Tectonics, Developments in Geotectonics*, vol. 25, edited by K. Olsen, pp. 427–436, Elsevier, The Netherlands, doi:10.1016/S0419-0254(06)80020-0.

Keller, G. R., and R. A. Stephenson (2007), The Southern Oklahoma and Dniepr-Donets aulacogens: A comparative analysis, in *4-D Framework of Continental Crust, Geological Society of America Memoir*, vol. 200, edited by R. D. Hatcher, M. P. Carlson, J. H. McBride, and J. R. M. Catalan, pp. 127–143, Int Basement Tecton Assoc, doi:10.1130/2007.1200(08), 17th International Conference on Basement Tectonics, Oak Ridge, TN, JUN 27-JUL 01, 2004.

Klein, G. D., and A. T. Hsui (1987), Origins of intracratonic basins, *Geology*, *17*, 1094–1098.

Korenaga, J., and S.-I. Karato (2008), A new analysis of experimental data on olivine rheology, *J. Geophys. Res.*, *113*, B02403, doi:10.1029/2007JB005100.

Koschmieder, E. (1966), On convection on a uniformly heated plane, *Beitr. Phys. Atmos.*, *39*, 1–11.

Lallemand, S., A. Heuret, and D. Boutelier (2005), On the relationships between slab dip, back-arc stress, upper plate absolute motion, and crustal nature in subduction zones, *Geochem. Geophys. Geosyst.*, *6*, Q09006, doi:10.1029/2005GC000917.

Levy, F., and C. Jaupart (2011), Temperature and rheological properties of the mantle beneath the North American craton from an analysis of heat flux and seismic data, *J. Geophys. Res.*, *116*, B01408, doi:10.1029/2010JB007726.

Lindsay, J. F., R. J. Korsch, and J. R. Wilford (1987), Timing the breakup of a Proterozoic supercontinent: Evidence from Australian intracratonic basins, *Geology*, *15*, 1061, doi:10.1130/0091-7613(1987)15<1061:TTBOAP>2.0.CO;2.

McKenzie, D., and K. Priestley (2008), The influence of lithospheric thickness variations on continental evolution, *Lithos*, *102*, 1–11, doi:10.1016/j.lithos.2007.05.005.

Michaut, C., C. Jaupart, and D. R. Bell (2007), Transient geotherms in Archean continental lithosphere: New constraints on thickness and heat production of the subcontinental lithospheric mantle, *J. Geophys. Res.*, *112*, B4408, doi:10.1029/2006JB004464.

Milelli, L., L. Fourel, and C. Jaupart (2012), A lithospheric instability origin for the Cameroon Volcanic Line, *Earth Planet. Sci. Lett.*, *335*, 80–87, doi:10.1016/j.epsl.2012.04.028.

Morel-à-l'Huissier, P., A. G. Green, and C. J. Pike (1987), Crustal refraction surveys across the Trans-Hudson Orogen/Williston Basin of south central Canada, *J. Geophys. Res.*, *92*, 6403–6420, doi:10.1029/JB092iB07p06403.

Nelson, K. D., et al. (1993), Trans-Hudson orogen and Williston basin in Montana and North Dakota: New COCORP deep-profiling results, *Geology*, *21*, 447, doi:10.1130/0091-7613(1993)021<0447:THOAWB>2.3.CO;2.

Parsons, B., and F. M. Richter (1980), A relation between the driving force and geoid anomaly associated with mid-ocean ridges, *Earth Planet. Sci. Lett.*, *51*, 445–450, doi:10.1016/0012-821X(80)90223-X.

Peslier, A. H., and J. F. Luhr (2006), Hydrogen loss from olivines in mantle xenoliths from Simcoe (USA) and Mexico: Mafic alkalic magma ascent rates and water budget of the sub-continental lithosphere, *Earth Planet. Sci. Lett.*, *242*, 302–319, doi:10.1016/j.epsl.2005.12.019.

Pollitz, F., G. Peltzer, and R. Burgmann (2000), Mobility of continental mantle: Evidence from postseismic geodetic observations following the 1992 Landers earthquake, *J. Geophys. Res.*, *105*, 8035–8054.

Poudjom Djomani, Y. H., S. Y. O'Reilly, W. L. Griffin, and P. Morgan (2001), The density structure of subcontinental lithosphere through time, *Earth Planet. Sci. Lett.*, *184*, 605–621, doi:10.1016/S0012-821X(00)00362-9.

Putirka, K. (2008), Excess temperatures at ocean islands: Implications for mantle layering and convection, *Geology*, *36*, 283–286, doi:10.1130/G24615A.1.

Reusch, A. M., A. A. Nyblade, D. A. Wiens, P. J. Shore, B. Ateba, C. T. Tabod, and J. M. Nnange (2010), Upper mantle structure beneath Cameroon from body wave tomography and the origin of the Cameroon Volcanic Line, *Geochem. Geophys. Geosyst.*, *11*, Q10W07, doi:10.1029/2010GC003200.

Reusch, A. M., A. A. Nyblade, R. Tibi, D. A. Wiens, P. J. Shore, A. Bekoa, C. T. Tabod, and J. M. Nnange (2011), Mantle transition zone thickness beneath Cameroon: Evidence for an upper mantle origin for the Cameroon Volcanic Line, *Geophys. J. Int.*, *187*, 1146–1150, doi:10.1111/j.1365-246X.2011.05239.x.

Rosenblat, S. (1982), Thermal convection in a vertical circular cylinder, *J. Fluid Mech.*, *122*, 395–410, doi:10.1017/S0022112082002274.

Saal, A. E., E. H. Hauri, C. H. Langmuir, and M. R. Perfit (2002), Vapour undersaturation in primitive mid-ocean-ridge basalt and the volatile content of Earth's upper mantle, *Nature*, *419*, 451–455.

Schutt, D. L., and C. E. Lesher (2006), Effects of melt depletion on the density and seismic velocity of garnet and spinel lherzolite, *J. Geophys. Res.*, *111*, B05401, doi:10.1029/2003JB002950.

Shapiro, N. M., M. H. Ritzwoller, J. C. Mareschal, and C. Jaupart (2004), Lithospheric structure of the canadian shield inferred from inversion of surface wave dispersion with thermodynamic a priori constraints, in *Geological Prior Information: Informing Science and Engineering*, vol. 239, edited by A. Curtis, and R. Wood, pp. 175–194, Geol. Soc. Spec. Publ., U.K., doi:10.1144/GSL.SP.2004.239.01.12.

Sleep, N. H., and A. M. Jellinek (2008), Scaling relationships for chemical lid convection with applications to cratonal lithosphere, *Geochem. Geophys. Geosyst.*, *9*, Q12025, doi:10.1029/2008GC002042.

Sloss, L. (1991), The tectonic factor in sea level change: A countervailing view, *J. Geophys. Res.*, *96*, 6609–6617.

Solomatov, V. S. (1995), Scaling of temperature- and stress-dependent viscosity convection, *Phys. Fluids*, *7*, 266–274, doi:10.1063/1.868624.

Solomatov, V. S., and L.-N. Moresi (2000), Scaling of time-dependent stagnant lid convection: Application to small-scale convection on Earth and other terrestrial planets, *J. Geophys. Res.*, *105*, 21,795–21,818, doi:10.1029/2000JB900197.

Stork, K., and U. Müller (1972), Convection in boxes: experiments, *J. Fluid Mech.*, *54*, 599–611.

Stork, K., and U. Müller (1975), Convection in boxes: An experimental investigation in vertical cylinders and annuli, *J. Fluid Mech.*, *71*, 231–240.

Tait, S., and C. Jaupart (1989), Compositional convection in viscous melts, *Nature*, *338*, 571–574, doi:10.1038/338571a0.

Thomas, W. A. (1991), The Appalachian-Ouachita rifted margin of southeastern North America, *Geol. Soc. Am. Bull.*, *103*(3), 415–431, doi:10.1130/0016-7606(1991)103<0415:TAORMO>2.3.CO;2.

Thomas, W. A. (2011), The Iapetan rifted margin of southern Laurasia, *Geosphere*, *7*, 97–120, doi:10.1130/GES00574.1.

Till, C. B., L. T. Elkins-Tanton, and K. M. Fischer (2010), A mechanism for low-extent melts at the lithosphere-asthenosphere boundary, *Geochem. Geophys. Geosyst.*, *11*, Q10015, doi:10.1029/2010GC003234.

Tokam, A.-P. K., C. T. Tabod, A. A. Nyblade, J. Julià, D. A. Wiens, and M. E. Pasyanos (2010), Structure of the crust beneath Cameroon, West Africa, from the joint inversion of Rayleigh wave group velocities and receiver functions, *Geophys. J. Int.*, *183*, 1061–1076, doi:10.1111/j.1365-246X.2010.04776.x.

de Vries, S. T., L. L. Pryer, and N. Fry (2008), Evolution of Neoarchean and Proterozoic basins of Australia, *Precambrian Res.*, *166*, 39–53, doi:10.1016/j.precamres.2008.01.005.

White, D. B. (1988), The planforms and onset of convection with a temperature-dependent viscosity, *J. Fluid Mech.*, *191*, 247–286, doi:10.1017/S0022112088001582.

Wilson, J. T. (1966), Did the Atlantic close and then reopen?, *Nature*, *211*, 676–681.